DOTTORATO DI RICERCA IN

FISICA

XVI CICLO

Sede Amministrativa

Università degli studi di MODENA e REGGIO EMILIA

TESI PER IL CONSEGUIMENTO DEL TITOLO DI DOTTORE DI RICERCA

Vertical Transport in Superlattices

CANDIDATO

Marcello Rosini

Contents

Introduction

Silicon is now experiencing a new phase as a functional material. In fact considerable effort is being devoted on the development of efficient silicon light emitting material [1, 2, 3, 4].

Light emission processes in silicon are clearly related to quantum confinement effects, thus Si devices based on confined structures, like quantum layers, quantum wires or quantum dots, have been the subject of intensive investigations by several research groups [2, 3, 4]. Silicon-based heterostructures form one of the most promising classes of such systems because of their easy compatibility with conventional silicon-based integrated circuit technology.

Superlattices, in particular, are quantum structures made of a periodic array of two alternating materials with different bandgaps such as, for example, Si/SiO_2 or Si/CaF_2. The alignement of the band edges for electrons (and holes) produces a periodic step-like potential that follows the structure of the superlattice. Superlattices were proposed, for the first time, by Esaki and Tsu in 1970, in order to observe Bloch oscillations. Superlattices are a suitable structure because the crystal period, along one direction, is considerably increased thus the length of the brillouin zone, along the same direction, is strongly reduced and high field effects, such as Bloch oscillations and negative differential conductivity, can be observed at lower electric field than in bulk materials. Due to the technological progress in growing tech-

niques such as molecular beam epitaxy (MBE) or chemical vapour deposition (CVD), nearly perfect layered low dimensional structures can be produced and quantum effects can be observed experimentally. Bloch oscillations have been observed experimentally in superlattices in 1992 [5] and nowadays superlattices are used for several kind of devices.

In particular Si/insulator multiple quantum wells or superlattices (SL), where calcium fluoride (CaF_2) or silicon dioxide (SiO_2) were used as insulating material, have been studied from both experimental and theoretical points of view, with a particular emphasis on their photoluminescence properties [6, 7, 8, 9, 10, 11, 12, 13, 14, 15, 16, 17, 18, 19, 20]. In these systems the thickness of the silicon layers lies in the nanometer range. It is interesting to note that most of the experimental work was originally based on amorphous silicon films; however well defined crystalline silicon superlattices are now available [21].

Beside photoluminescence, also electroluminescence has been observed both in Si/CaF_2 and Si/SiO_2 superlattices [22, 23, 24, 25, 26, 27]. Since the optimization of the electroluminescence is related to the carrier injection efficiency into the Si quantum layers, it is very important to understand the electrical transport properties of these structures. Until now this has been performed by computing current-voltage characteristics both for Si/CaF_2 [28, 29] and Si/SiO_2 [30] multiple quantum wells through model calculations, where electron and hole tunneling between adjacent wells is evaluated within the Wentzel-Kramers-Brillouin approximation [31] or by modeling charge carrier transport across the heterostructures by means of an equivalent circuit [32]. From the numerical results a number of simple conclusions useful to optimize physical parameters in order to achieve their maximum electroluminescence efficiency has been derived.

Our aim here is to investigate the transport properties of Si/SiO_2 superlattices through a Monte Carlo simulator in order to study the best response

to an applied electric field. In the first chapter, the theoretical framework used for calculating the electronic structure and the electron-phonon interaction probability is presented. The second chapter concerns vertical transport in the system under investigation while chapter 3 describes transport phenomena in the same superlattice, when a parallel component is added to the vertical electric field. This simulation is performed using a miniband transport approach.

Some considerations [33] about the particular structure and the electric fields applied lead to identify different transport regimes, in particular it can be deduced that the miniband transport approach is not a suitable description for high electric fields and a different description is needed for a transport study. The fourth chapther is an investigation of transport using the quantum description of the electronic states provided by the Wannier-Stark functions. Then, a description of a proposal for obtaining a superlattice based device, able to have high electroluminescence, is described.

The last chapter is very different from the main topic of the thesis. An investigation of single electron transport in quantum wires is performed. In particular, the simulated device has been proposed in order to perform the basic operations needed for quantum computation and a surface acoustic wave potential has been introduced in order to study its effect on the functionality of the device. A more specific introduction to this argument is provided in the first section of the chapter.

Part I

Transport in superlattices

Chapter 1

Superlattice bands and phonons

The aim of this chapter is to present the theoretical modeling of a low-dimensional structure. In particular, in order to perform transport calculations, we need to know electrical and vibrational properties of the structure under investigation. In order to describe the electronic structure of the superlattice, we have chosen the envelope function approximation, while the vibrational properties are described within the confined optical phonon framework.

1.1 The envelope-function approximation

Let us consider an electron moving in a superlattice defined by the periodic potential $\widehat{U}_{SL}(z)$, the complete Hamiltonian of the system is

$$\widehat{H} = -\frac{\hbar^2}{2m_e}\widehat{\mathbf{k}}^2 + \widehat{V}_{cr}(\mathbf{r}) + \widehat{U}_{SL}(z) \tag{1.1}$$

where $\widehat{V}_{cr}$ is the crystal potential. We make the assumption that the crystal potential $\widehat{V}$ is the same all over the superlattice and, therefore, that the changes in the different materials are included in the $\widehat{U}_{SL}(z)$ term.

It is possible to suppose, for the wave function of the system, an expansion

using the solutions (Bloch functions) of the crystalline potential, as follows:

$$|\Psi\rangle = \sum_{n',\mathbf{k}'} C_{n',\mathbf{k}'} |\psi_{n',\mathbf{k}'}\rangle \tag{1.2}$$

then, substituting this wave function into the Schrödinger equation $\widehat{H}(\mathbf{r})|\Psi\rangle = E|\Psi\rangle$ an multiplying by $\langle\psi_{n,\mathbf{k}}|$, we obtain

$$E_n(\mathbf{k})C_{n,\mathbf{k}} + \sum_{n',\mathbf{k}'} C_{n',\mathbf{k}'} \langle\psi_{n,\mathbf{k}}|\widehat{U}|\psi_{n',\mathbf{k}'}\rangle = EC_{n,\mathbf{k}'} \ . \tag{1.3}$$

The term in the sum can be analyzed writing down the Fourier expansion of the periodic superlattice potential $\widehat{U}(\mathbf{r}) = \sum_{\mathbf{G}} \widehat{U}_{\mathbf{G}} e^{i\mathbf{G}\mathbf{r}}$, where $\mathbf{G}$ are the vectors in the reciprocal superlattice space. With this substitution the above equation becomes

$$\langle\psi_{n,\mathbf{k}}|\widehat{U}|\psi_{n',\mathbf{k}'}\rangle = \frac{1}{NV_0} \sum_{\mathbf{G}} U_{\mathbf{G}} \sum_{\boldsymbol{n}} e^{i(\mathbf{k}-\mathbf{k}'+\mathbf{G})\boldsymbol{n}} \langle u_{n,\mathbf{k}}|u_{n',\mathbf{k}'}\rangle \ , \tag{1.4}$$

where u is the periodic part of the Bloch function, andV_0 is the volume of the unit cell. Now, taking into account the properties of the delta function that arises from the sum $\frac{1}{N}\sum e^{i(\mathbf{k}-\mathbf{k}'+\mathbf{G})\boldsymbol{n}} = \delta_{\mathbf{k}',\mathbf{k}+\mathbf{G}}$, and defining the quantity $\Delta^{n,n'}_{\mathbf{k},\mathbf{k}+\mathbf{G}} = \frac{1}{V_0}\langle u_{n,\mathbf{k}}|u_{n',\mathbf{k}+\mathbf{G}}\rangle$, the eq. 1.3 now can be written

$$E_n(\mathbf{k})C_{n,\mathbf{k}} + \sum_{n',\mathbf{k}-\mathbf{G}} U_{\mathbf{G}} C_{n',\mathbf{k}+\mathbf{G}} \Delta^{n,n'}_{\mathbf{k},\mathbf{k}+\mathbf{G}} = EC_{n,\mathbf{k}} \ . \tag{1.5}$$

Now, the first approximation is to suppose

$$\Delta^{n,n'}_{\mathbf{k},\mathbf{k}+\mathbf{G}} \simeq \Delta^{n,n'}_{\mathbf{k},\mathbf{k}} = \delta_{n,n'} \ . \tag{1.6}$$

In other words we neglect interband interactions; moreover, we suppose that the product $\langle u_{n,\mathbf{k}}|u_{n',\mathbf{k}+\mathbf{G}}\rangle$ does not change appreciably for different $\mathbf{G}$. Within this approximation the initial Schrödinger equation (1.3) is now:

$$E_n(\mathbf{k})C_{n,\mathbf{k}} + \sum_{\mathbf{G}} \widehat{U}_{\mathbf{G}} C_{n,\mathbf{k}-\mathbf{G}} = EC_{n,\mathbf{k}} \ . \tag{1.7}$$

The eigenstate 1.2 is to be modified according to the hypothesis that electrons are near a band minimum, and that we are neglecting interband interactions. We can thus write

$$|\Psi\rangle \simeq \sum_{\mathbf{k}} C_{n,\mathbf{k}}|\psi_{n,\mathbf{k}}\rangle = \sum_{\mathbf{k}} C_{n,\mathbf{k}} e^{i\mathbf{kr}}|u_{n,\mathbf{k}}\rangle \simeq \mathcal{F}_n(\mathbf{r})|u_{n,\mathbf{k}_0}\rangle \ , \tag{1.8}$$

$$\mathcal{F}_n(\mathbf{r}) = \frac{1}{\sqrt{V_0}} \sum_{\mathbf{k}} e^{i\mathbf{kr}} C_{n,\mathbf{k}} \ , \tag{1.9}$$

having introduced the envelope function $\mathcal{F}$. By applying the Fourier antitrasform to eq. 1.7, we obtain the Schrödinger equation whose solution is the envelope function

$$\left[\widehat{E}_n(-i\nabla) + \widehat{U}(\mathbf{r})\right] \mathcal{F}_n(\mathbf{r}) = E\mathcal{F}_n(\mathbf{r}) \ ; \tag{1.10}$$

in this equation, $\widehat{E}_n(-i\nabla)$ is the energy operator of the crystal, that, within the parabolic band approximation, turns out to be [34]

$$\widehat{E}_n(-i\nabla) \simeq E_n(\widehat{\mathbf{k}}_0) + \frac{\hbar^2}{2}\widehat{k}_i \left(\frac{\hbar^2}{2m^*}\right)_{i,j} \widehat{k}_j \ . \tag{1.11}$$

In this last formula, $\left(\frac{\hbar^2}{2m^*}\right)_{i,j}$ is the inverse effective mass tensor, that corresponds to the curvature of the band in $\mathbf{k}_0$ and describes the parabolic approximation of the band shape near this point. Thus, the final equation to solve is (we neglect the constant energy term)

$$\left(\frac{\hbar^2}{2}\nabla\frac{1}{m^*}\nabla + \widehat{U}(z)\right) \mathcal{F} = E\mathcal{F} \ , \tag{1.12}$$

that is a crystal-like equation. This equation describes the motion of an electron of mass m^* in a periodic potential $\widehat{U}$, and the envelope function $\mathcal{F}$ is the Bloch eigenstate of this Hamiltonian. From a mathematical point of view, the envelope function really envelopes the crystal periodic part u of the Bloch function.

Now we can approcah the problem of the superlattice potential. The physical meaning of the envelope function is evident in Fig.1.1.

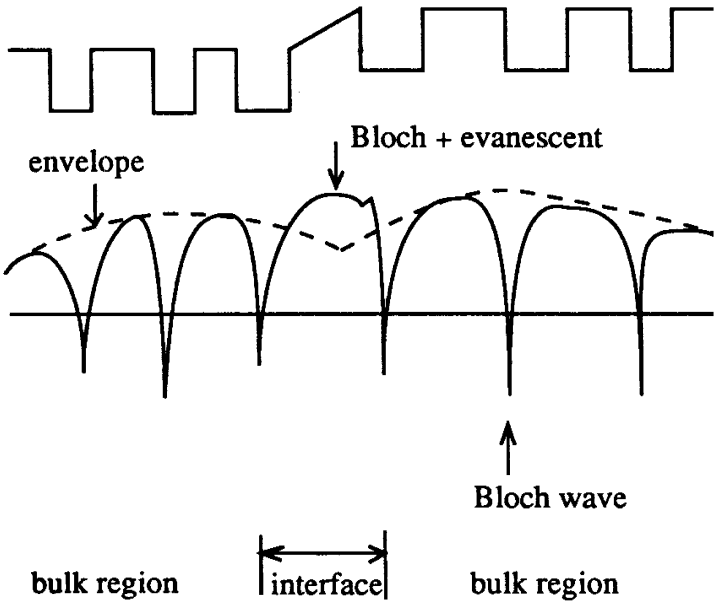

Figure 1.1: *Physical meaning of the envelope function: the envelope function (dashed line) is the mathematical envelope of the Bloch wave (continuous line) of the superlattice. Moreover the interface boundary condition is shown. (From [35])*

1.2 Current conserving boundary conditions

In a superlattice, the potential $\widehat{U}$ is obtained with the superposition of different materials. This superposition gives rise to a sharp interface potential, owing to the different conduction band energies. The conduction-band effective mass tensor will be, in general, different in the two materials (m_a for the first material and m_b for the second one), then it is easy to understand that the interface continuity of the derivative of the wave function $\nabla\psi_a = \nabla\psi_b$ is no longer the right condition since the current is not conserved:

$$\vec{J}_a = -\frac{i\hbar}{m_a}\mathrm{Re}\left(\psi_a^*\nabla\psi_a\right) \tag{1.13}$$

$$\vec{J}_b = -\frac{i\hbar}{m_b}\mathrm{Re}\left(\psi_b^*\nabla\psi_b\right) \ , \tag{1.14}$$

are different.

If we look at eq. 1.12, we have to introduce the right z-dependence to the

effective mass, then the system Hamiltonian is now

$$\widehat{H}^{\star} = -\frac{\hbar^2}{2}\nabla\frac{1}{m(z)}\nabla + \widehat{U}(\mathbf{r}) \ , \tag{1.15}$$

From which the new current conserving boundary condition at the interfaces can be deduced:

$$\frac{1}{m_a}\nabla\psi_a(\mathbf{r}_0) = \frac{1}{m_b}\nabla\psi_b(\mathbf{r}_0) \ . \tag{1.16}$$

In order to obtain the right solution of the superlattice potential, this condition has to be used together with the continuity of the wave function at the interface. From these copnditions $\vec{J_a}$ and $\vec{J_b}$ as given in eq.(1.13) and (1.14) are equal.

1.3 Solution of the Krönig-Penney potential

As introduced in the previous section, the superlattice potential is determined by the conduction band offset of the materials used. In particular, if we consider intrinsic semiconductors with sharp interfaces, band bending at the interfaces can be neglected and the structure potential $\widehat{U}$ in eq. 1.15 can be modeled using a Krönig-Penney square-well potential:

$$\widehat{U}(z) = \begin{cases} 0 \ , & -b \leq z \leq 0 \\ U_0 \ , & 0 \leq z \leq a \end{cases} \ , \tag{1.17}$$

whose solution can be written, in the general case, as

$$\psi(z) = \begin{cases} \psi_a(z) = A_a \sin(\alpha z) + B_a \cos(\alpha z) \ , & 0 \leq z \leq a \\ \psi_b(z) = A_b \sin(\beta z) + B_b \cos(\beta z) \ , & -b \leq z \leq 0 \end{cases} \tag{1.18}$$

where $\alpha^2 = \frac{2m_a}{\hbar^2}E$ and $\beta^2 = \frac{2m_b}{\hbar^2}(E - V_0)$; in the energy range where $\beta < 0$ the solution is written in terms of hyperbolic functions, so it follows an exponential behavior. Now the current and wave function continuity have to be taken into account. An other condition derives from the consideration

that the superlattice potential is periodic and the wave function has to obey the Born-Von Karman condition of periodicity $\psi(z+Nd)=\psi(z)$; thus it is possible to verify a Bloch theorem that states

$$\psi(z+nd)=C_n\psi(z)=e^{iqnd}\psi(z)=e^{ik_zd}\psi(z)\ , \tag{1.19}$$

where $k_z=qn=\frac{2\pi}{Nd}n$ is the pseudomomentum along the z direction of the superlattice minizone.
The linear system resulting from these conditions is

$$\begin{cases} B_a=B_b \\ \frac{\alpha}{m_a}A_a=\frac{\beta}{m_b}A_b \\ A_a\sin(\alpha a)+B_a\cos(\alpha a)=e^{iq(a+b)}\left[-A_b\sin(\beta b)+B_b\cos(\beta b)\right] \\ \frac{\alpha}{m_a}A_a\cos(\alpha a)-\frac{\alpha}{m_a}B_a\sin(\alpha a)=e^{iq(a+b)}\left[\frac{\beta}{m_b}A_b\cos(\beta b)+\frac{\beta}{m_b}B_b\sin(\beta b)\right] \end{cases} . \tag{1.20}$$

As usual, the only non trivial solution of the system exists when the determinant of the coefficient is zero: this secular equation is

$$\cos q(a+b)=\cos(\alpha a)\cos(\beta b)-X\sin(\alpha a)\sin(\beta b) \tag{1.21}$$

with $X=\frac{\alpha^2m_b^2+\beta^2m_a^2}{2\alpha\beta m_am_b}$.
When $E<U_0$ (the barrier height) we can write $\beta=i\beta_-$ obtaining the new expression for the above equation

$$\cos q(a+b)=\cos(\alpha a)\cosh(\beta_-b)-X\sin(\alpha a)\sinh(\beta_-b) \tag{1.22}$$

where now $X=\frac{\alpha^2m_b^2-\beta_-^2m_a^2}{2i\alpha\beta_-m_am_b}$.

1.4 Band structure

The equation derived in the previous section has no analytical solution and it has been solved with numerical methods. An approximated analytical

solution, very useful for transport calculations, is provided by the tight-binding theory. This method is in general used to calculate crystal band structure and we can successfully apply it to our superlattice problem by treating every quantum well of the structure as a crystal cell, as shown in the previous sections.

The central idea of this approach is to consider infinitely far quantum wells, so that they cannot interact with each other. In this situation, the solution is an infinite set of degenerate levels, and the single-quantum-well problem is represented by the following Hamiltonian

$$\left[\widehat{T} + \widehat{V}(z - nd)\right] \chi_j(z - nd) = \epsilon_j \chi_j(z - nd) \ , \tag{1.23}$$

where n is the index of the well and j leabels the well state. When the distance d between the wells is reduced, their mutual interaction is no longer negligible and the degeneracy disappears giving rise to a continuum energy band. It is now sensible to guess for the many-quantum-well wave function a combination of single-well solutions

$$\Psi_{j,k_z}(z) = \sum_n e^{ik_z nd} \chi_j(z - nd) \ . \tag{1.24}$$

It is easy to show that this function satisfies the Bloch theorem. In the following a one-band model is taken into account, and the Dirac formalism is introduced, so that the wave function are now written $\Psi_{j,k_z}(z) = |\Psi\rangle$, $\chi_j(z - nd) = |z - nd\rangle$. Now it is useful to introduce in the Hamiltonian the potential as the sum of all the square well potential

$$\widehat{V}_{SR}(z) = \widehat{V}(z - nd) + \sum_{l \neq n} \left[\widehat{V}(z - ld) - V_0\right] \ , \tag{1.25}$$

and multiplying by $\langle z - md|$, after simple calculations we get to the following result:

$$\begin{aligned} &\sum_n \sum_{l \neq n} e^{ik_z nd} \langle z - md|\widehat{V}(z - ld)|z - nd\rangle = \\ &= [E_j(k_z) - \epsilon_j] \sum_n e^{ik_z nd} \langle z - md|z - nd\rangle \ . \end{aligned} \tag{1.26}$$

The key point of the tight-binding approach is to neglect next-nearest-neighbor coupling; this hypothesis is reasonable when barriers are sufficiently strong to confine the single-well wave function mostly into only one well; moreover, since the above Hamiltonian is invariant for translations, we can consider $n = 0$. This means that the indexes can assume values only $m,\ l = -1,\ 0,\ +1$. The remaining terms can be rewritten, using symmetry considerations, with the notation

$$r_j = \langle z|z-d\rangle = \langle z|z+d\rangle \tag{1.27}$$

$$s_j = \langle z|\widehat{V}(z-d)|z\rangle = \langle z|\widehat{V}(z+d)|z\rangle \tag{1.28}$$

$$t_j = \langle z|\widehat{V}(z)|z-d\rangle = \langle z|\widehat{V}(z)|z+d\rangle\ . \tag{1.29}$$

These terms are, respectively, the overlap integral, the shift integral and the transfer integral. In general the overlap term is negligible with respect to the other terms, so the final form for the miniband is now

$$E_j(k_z) = \epsilon_j - s_j - 2t_j\cos(k_z d)\ . \tag{1.30}$$

Moving now to three dimensions, the Schrödinger equation is

$$\widehat{H} = \widehat{\mathbf{p}}_i \frac{1}{2m^*_{i,j}} \widehat{\mathbf{p}}_j + \widehat{U}(z)\ . \tag{1.31}$$

Since the potential energy $\widehat{U}$ depends only on the growing direction z of the superlattice, the problem can be separated along the three space directions, resulting in two free-particle equations, along the xy plane, and a Krönig-Penney problem along the growing direction. The solution of the problem can be written as

$$\Psi_{j,k_z}(\mathbf{r}) = \mathcal{F}_{j,k_z}(z)e^{-i(k_x x + k_y y)}\ , \tag{1.32}$$

$$E_j(\mathbf{k}) = E_j(k_z) + \frac{\hbar^2}{2m_x}k_x^2 + \frac{\hbar^2}{2m_y}k_y^2 \tag{1.33}$$

where the envelope function $\mathcal{F}_{j,k_z}(z)$ and the energy $E_j(k_z)$ are solution of the Krönig-Penney potential. In particular the envelope function is obtained

with computer calculation while for the energy spectrum the Tight-Binding model is used

$$E_j(k_z) = \tilde{\epsilon}_j - \tilde{t}_j \cos(k_z d) \; ; \tag{1.34}$$

in this form we have defined $\tilde{\epsilon}_j = \epsilon_j - s_j$ as the central energy of the miniband, and $\tilde{t}_j = 2t_j$ its half amplitude.

Since the aim of this work is to study transport properties of $Si(100)/SiO_2$ superlattices, the particular band structure of silicon has to be taken into account. The ellipsoidal shape of the band minima is accounted for by the different effective masses in eq.(1.33). Moreover, the bulk silicon band structure shows six different energy minima, located along the (100) symmetry directions, at 0.8 G from Γ point. Since the growing direction of the superlattice is the (001) direction of Si, the effective mass tensor results to be diagonal in the superlattice coordinates and the Hamiltonian is still separable along these directions (the case of silicon grown along any direction is treated in appendix B.1). The eq.(1.33) has to be applied to each of the six band minima of silicon, then the more general expression for the superlattice miniband structure is now:

$$E_j^\alpha(\mathbf{k}) = \frac{\hbar^2}{2m_x}(k_x^2 - k_{x,0}^\alpha) + \frac{\hbar^2}{2m_y}(k_y^2 - k_{y,0}^\alpha) + \left[\tilde{\epsilon}_j^\alpha - \tilde{t}_j^\alpha \cos(k_z d)\right] \tag{1.35}$$

where $\mathbf{k}_0^\alpha$ is the coordinate of the minimum of the α-th valley of silicon, $\tilde{\epsilon}_j^\alpha$ and $\tilde{t}_j^\alpha$ are obtained from the Krönig-Penney model for each valley.

It is easy to understand that the four minima located along the x and y directions remain in the same position, while the two minima along the growing direction do not: they are refolded into the same (double degenerate) miniband at $z = 0$ owing to the superlattice potential. The energy dispersion obtained with the above theory for the $Si(100)/SiO_2$ superlattice is represented in Fig.1.2.

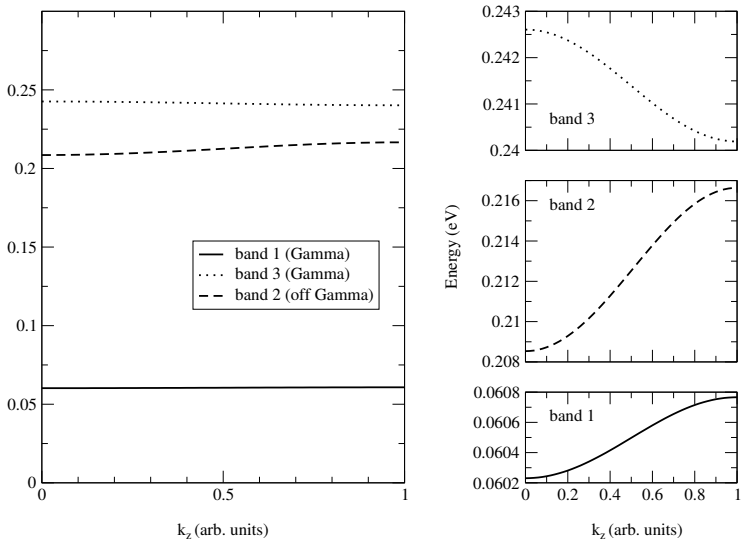

Figure 1.2: *k_z dispersion of the minibands. The dashed line represents the z dispersion of the (100) and (010) valleys. Note the different scales in the three figures on the right showing enlargements on the minibands.*

1.4.1 Tunneling effective mass

In order to solve the energy problem for the Si/SiO_2 superlattice, the current-conserving boundary condition has to be satisfied: this means that we have to find out a value for the electron effective mass in the SiO_2 regions. In particular, in our calculation, the barrier energy is higher than the electron energy, so it is impossible to define the effective mass for the oxide layer, in the traditional way as the band curvature, since there is no band. On the other hand, experiments have been performed measuring the tunneling current through oxide barriers where the effective mass is used as a parameter to fit theory on the experimental results. This value is called "tunneling effective mass", and takes into account all the interactions, due to the barrier material, that are not explicitly included in the theory. Some values found in the literature are $m^* = (0.29 \pm 0.02)\ m_{el}$ [36], $m^* = (0.30 \pm 0.02)\ m_{el}$ [37].

In our calculation we use $m^* = 0.30\ m_{el}$.

1.5 Electron-phonon interaction

In order to make a complete study of the transport properties of the system, the analysis of the scattering mechanisms, acting on electron motion, is required.

In principle we can suppose that the superlattice is characterized by sharp interfaces between the two materials that compose it, thus eliminating the effect of the surface roughness. Moreover, since we consider the superlattice made with intrinsic semiconductors, it is possible to neglect impurity scattering. The carrier-carrier scattering is not included in this model since it is not relevant at the carrier concentration used in this work. The only scattering mechanism introduced in the model is the optical phonon scattering. Acoustic phonons are not taken into account because their scattering rate is much lower than optical phonon rate, at the simulated temperature.

Optical phonons in superlattices are generally confined [38]. This means that the silicon layers will show optical frequencies typical of bulk silicon and oxide layers will behave like bulk oxide. We can explain this behavior thinking abut the properties of phonons: the dispersion of optical phonon modes is almost flat so it is possible to define a very narrow energy region, typically identified with a single energy value. This energy is generally different for different materials, in particular silicon and silicon dioxide show very different phonon energies. This means that a phonon mode propagating in silicon with a particular energy, cannot propagate through a SiO_2 layer because the motion at the same energy is forbidden. This situation is equivalent to a mechanical boundary condition. Moreover, since the phonon branch is very flat, the corresponding group velocity is very low and the lattice excitation does not propagate along the material and the vibration remains confined

within the same layer. This picture results close to the einstein model for phonons. A representation of phonon modes is provided in Fig.(1.3) where it is possible to observe confining and interface decay of optical phonons in Si/Ge superlattices.

Since SiO_2 is a polar material, polar optical phonons will be included due to oxide slabs, while for silicon we have to take into account only deformation potential phonons.

The electron-optical phonon interaction is treated using the time-dependent perturbation theory in both semiclassical and Wannier-Stark transport calculations. The complete Hamiltonian is

$$\widehat{H} = \widehat{H}_{SL} + \widehat{H}'_{e-ph} \tag{1.36}$$

where $\widehat{H}_{SL}$ is the effective hamiltonian for the electron in the superlattice

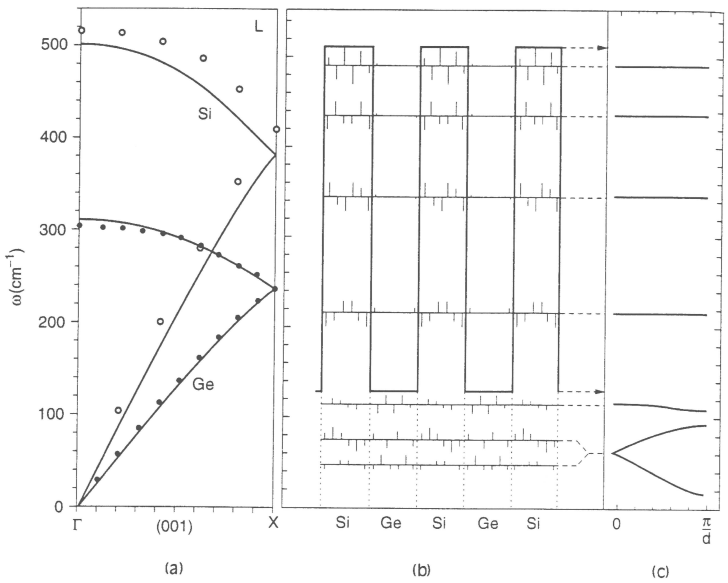

Figure 1.3: *Representation of optical phonon confinement. From this figure it can be deduced that optical phonons are confined in the layers while acoustic phonons are extended in the whole system. From [39]*

potential, and $\widehat{H}'_{e-ph}$ is the electron-phonon interaction

$$\widehat{H}'_{e-ph} = \sum_q c(q) \left(a_{\mathbf{q}} e^{i\mathbf{qr}} + a^{\dagger}_{\mathbf{q}} e^{-i\mathbf{qr}} \right) , \tag{1.37}$$

according to the Frölich theory [40]. For deformation potential and polar potential respectively we have

$$c^2_{def}(\mathbf{q}) = \frac{\hbar e^2 \omega}{2V\epsilon_0} \left(\frac{1}{\epsilon_+} - \frac{1}{\epsilon_-} \right) \frac{\mathbf{q}^2}{(\mathbf{q}^2 - \mathbf{q}_D^2)^2} \tag{1.38}$$

$$c^2_{pol}(\mathbf{q}) = \frac{\hbar (D_t k)^2}{2V\omega\rho} \tag{1.39}$$

where ω is the phonon frequency, ϵ_+, ϵ_- are the high and low frequency relative dielectric constant, $\mathbf{q}_D$ is the screening wave vector, $D_t k$ the deformation potential coupling with phonons, V is the crystal volume and ρ is the material density. Detailed calculation of the transition rates will be performed in the following chapters.

Since silicon is a non-polar material, electrons will interact with the lattice only via the deformation potential.

In silicon dioxide, two polar optical modes are present at different energies, with different coupling constants. These two modes are introduced in the simulations as a single mode at intermediate energy with coupling constant equal to the sum of the original constants.

Chapter 2

Vertical transport in Si/SiO_2 superlattices - Extended states

2.1 Transport phenomena in superlattices

The sinusoidal shape of the miniband, and the reduced dimension of the Brillouin zone, give rise to two important phenomena, typical of the superlattice structure that we are now going to describe: Bloch oscillations and negative differential conductivity.

Let us consider an electron in a one-dimensional miniband, with an electric field applied along this direction z. Using a semiclassical aproximation for the electron, such that the wave packet is well localized both in real and in reciprocal space, we can describe the motion of the electron as a semiclassical particle where

$$\hbar \frac{\mathrm{d}k}{\mathrm{d}t} = -eE \tag{2.1}$$

and the energy of the particle is the miniband $\epsilon(k)$. If the electric field is constant in time, the solution is

$$k(t) = k_0 + \frac{eE}{\hbar} t \ , \tag{2.2}$$

that is the wave vector increases linearly with time. If no scattering mechanism is present, the electron travels through the whole minizone in a time

$$T_B = \frac{2\pi/d}{eE/\hbar} , \tag{2.3}$$

and when it is at the minizone boundary, the electron wave vector is changed by a reciprocal lattice vector. In this way, the wave vector will appear at an opposite point of the minizone nd the process will repeat. The resulting motion will have an oscillatory behavior and this phenomenon is known as *Bloch oscillation*. The law of motion can be calculated using the miniband shape (eq.1.34)

$$\begin{aligned} z(t) &= \int_0^t v(t')\mathrm{d}t' \\ &= \int_0^t \frac{1}{\hbar}\frac{\mathrm{d}\epsilon(k(t'))}{\mathrm{d}k}\mathrm{d}t' \\ &= \frac{\widetilde{t}d}{\hbar}\int_0^t \sin\left(\frac{eE}{\hbar}dt'\right)\mathrm{d}t' \\ &= \frac{\widetilde{t}}{eE}\left[1-\cos(\omega_B t)\right] . \end{aligned} \tag{2.4}$$

This equation describes an harmonic oscillation in real space, with an amplitude

$$\Lambda = \frac{\widetilde{t}}{eE} . \tag{2.5}$$

It is evident that this amplitude depends upon the miniband width and the applied electric field: with higher field, the oscillation becomes more localized in space.

As said before, the Bloch oscillation occurs in absence of scattering mechanisms, or, at least, with a scattering rate lower than the period of the oscillation. This condition can be written as

$$\omega_B\bar{\tau} \gg 1 . \tag{2.6}$$

where $\bar{\tau}$ is the mean scattering time and $\omega_B = \frac{2\pi}{T_B}$.

Bloch oscillations where predicted by Bloch in 1928 [41], but they have not been observed until 1992 [5]. The reason is that before superlattices were built, the Brillouin zones were not sufficiently narrow to fulfill the above condition (eq.2.6). Moreover the low dimensionality of such structures has the effect of lowering the strength of the scattering mechanism, thus increasing $\bar{\tau}$.

The other phenomenon that typically occurs in superlattices is the negative differential conductivity at high electric fields. The first theory proposed to describe band transport with scattering mechanisms in superlattices was developed in 1970 by Esaki and Tsu [42]. In their one dimensional picture, each scattering event is supposed to dissipate entirely the electron energy and momentum, so the carrier is scattered to the center of the minizone. This interaction occurs with a mean time τ_{ET}, dependent on on the scattering mechanism and temperature. If the electric field is low, electrons are scattered before reaching the zone boundary, but when the field increases, they can perform one or more Bloch oscillations before being scattered, so the drift velocity decreases at high electric fields. This is known as the *negative differential conductivity (NDC)* regime[1].

The probability that an electron in a state k is scattered after a time t within the time dt is $P[k(t)]\mathrm{d}t = e^{-\frac{t}{\tau}\frac{\mathrm{d}t}{\tau}}$ (this is the product of the probability to have not been scattered until time t and to suffer a scattering within time interval dt) and the mean velocity of the electron can be obtained by integrating the phase velocity in time, using this probability:

$$\begin{aligned} v_{ET} &= \int_0^\infty v e^{-\frac{t}{\tau_{ET}}} \frac{\mathrm{d}t}{\tau} \\ &= \int_0^\infty e^{-\frac{t}{\tau_{ET}}} \frac{1}{\hbar\tau} \frac{\mathrm{d}\epsilon[k(t)]}{\mathrm{d}k} \mathrm{d}t \end{aligned}$$

[1] This NDC is a different phenomenon with respect to the one due to the presence of upper valleys

$$= \frac{\tilde{t}d}{\tau\hbar}\int_0^\infty e^{-\frac{t}{\tau_{ET}}}\sin\omega_B t\,\mathrm{d}t$$
$$= \frac{v_{max}}{\omega_B\tau_{ET}+(\omega_B\tau_{ET})^{-1}}\ , \tag{2.7}$$

where eq.(2.2) has been used and $v_{max}=\frac{\tilde{t}d}{\hbar}$. At low electric field ($\omega_B\tau_{ET}\ll 1$) the first denominator term can be neglected and the velocity is

$$v_{ET\downarrow} = v_{max}\omega_B\tau_{ET} = \frac{e\tilde{t}d^2\tau}{\hbar^2}E \tag{2.8}$$

while for high fields ($\omega_B\tau_{ET}\gg 1$)

$$v_{ET\uparrow} = \frac{v_{max}}{\omega_B\tau_{ET}} = \frac{\tilde{t}}{e\tau}\frac{1}{E}\ . \tag{2.9}$$

The highest drift velocity is obtained at $\omega_B\tau_{ET}=1$, the corresponding electric field is $E_c=\frac{\hbar}{e\tau_{ET}}$ and the value is $\bar{v}=\frac{v_{max}}{2}$. It is possible to write the drift velocity as:

$$\frac{1}{v_{ET}} = \frac{1}{v_{ET\downarrow}} + \frac{1}{v_{ET\uparrow}}\ . \tag{2.10}$$

2.2 Phonon transition probabilities

Phonon scattering is treated within the first-order time-dependent perturbation theory using the Fermi Golden Rule

$$P(n,\mathbf{k};n',\mathbf{k}') = \frac{2\pi}{\hbar}\left|\langle n',\mathbf{k}'|\widehat{H}'|n,\mathbf{k}\rangle\right|^2\delta\left[E_{n'}(\mathbf{k}')-E_n(\mathbf{k})\right]\ . \tag{2.11}$$

For simplicity we can indicate $M_{ij}(\mathbf{k}\mathbf{k}')=\langle j,\mathbf{k}'|\widehat{H}'|i,\mathbf{k}\rangle$ that describes the particular scattering mechanism. In order to obtain the total scattering probability for an electron in the state $(i,\mathbf{k})$[2] with every final state $(j,\mathbf{k}')$, the equation above has to be integrated over $\mathbf{k}'$ and to be summed over j:

$$\Gamma_i(\mathbf{k}) = \frac{2\pi}{\hbar}\sum_j\frac{V}{(2\pi)^3}\int|M_{i,j}(\mathbf{k},\mathbf{k}')|^2\delta\left(E_j(\mathbf{k}')-E_i(\mathbf{k})\mp\hbar\omega_{\pm(\mathbf{k}'-\mathbf{k})}\right)\mathrm{d}\mathbf{k}'\ . \tag{2.12}$$

[2] i is the miniband number and $\mathbf{k}$ is the pseudo-momentum in the minizone

The following calculation will be performed supposing that the matrix element M is independent of $\mathbf{k}'$ since, as we will see, this is the general case for our simulation (the specific dependence upon $\mathbf{k}'$ will be taken into account in succecive step of the simulation). Moreover, since we are including only optical phonon scattering, $\omega_{\pm(\mathbf{k}'-\mathbf{k})} = \omega_{op}$ can be considered constant all over the Brillouin zone. We do not calculate the sum over the band index, since we are interested in the total scattering probability separately for each final-state miniband. The total scattering probability now becomes

$$\Gamma_{ij}(\mathbf{k}) = \frac{2\pi}{\hbar}|M_{i,j}|^2 \frac{V}{(2\pi)^3} \int \delta\left(E_j(\mathbf{k}') - E_i(\mathbf{k}) \mp \hbar\omega_{op}\right) \mathrm{d}\mathbf{k}' \ . \tag{2.13}$$

Using the standard definition for the density of states, and using the energy E as variable, the above expression becomes

$$\Gamma_{ij}(E) = \frac{\pi}{\hbar}|M_{i,j}|^2 \mathrm{DOS}_j(E \pm \hbar\omega_{op}) \ . \tag{2.14}$$

The development of the calculation for $\mathrm{DOS}_j(E)$ is shown in the following, where by using the miniband expression calculated in eq.(1.35), and applying the following ellipsoidal transformation

$$T : \begin{cases} \frac{1}{\sqrt{m_x^j}}(k_x - k_{0,x}^j) &= \frac{1}{\sqrt{m_0}} k_{\parallel} \cos\vartheta \\ \frac{1}{\sqrt{m_y^j}}(k_y - k_{0,y}^j) &= \frac{1}{\sqrt{m_0}} k_{\parallel} \sin\vartheta \\ k_z^j &= k_{\perp} \end{cases} \tag{2.15}$$

we now obtain

$$\begin{aligned} &\mathrm{DOS}_j(E) = \\ &= \frac{V}{4\pi^3} \frac{\sqrt{m_x^j m_y^j}}{m_0} \int \mathrm{d}\vartheta \int \mathrm{d}k_{\perp} \int \delta\left[E - \frac{\hbar^2}{2m_0}k_{\parallel}^2 - \epsilon^j + t^j \cos(k_z d)\right] k_{\parallel} \mathrm{d}k_{\parallel} \\ &= \frac{V\sqrt{m_x^j m_y^j}}{2\pi^2\hbar^2} \int \mathrm{d}k_{\perp} \int \delta\left[E - \frac{\hbar^2}{2m_0}k_{\parallel}^2 - \epsilon^j + t^j \cos(k_z d)\right] \mathrm{d}\left(\frac{\hbar^2 k_{\parallel}^2}{2m_0}\right) \\ &= \frac{V\sqrt{m_x^j m_y^j}}{2\pi^2\hbar^2} \int \mathrm{d}k_{\perp} \int_0^{\infty} \delta\left[E - Y - \epsilon^j + t^j \cos(k_z d)\right] \mathrm{d}Y \ , \end{aligned} \tag{2.16}$$

and integrating along the variable $Y = \frac{\hbar^2 k_{\parallel}^2}{2m_0}$ we get the density of states as

$$\mathrm{DOS}_j(E) = \frac{V\sqrt{m_x^j m_y^j}}{2\pi^2\hbar^2} \int_{-\frac{\pi}{d}}^{\frac{\pi}{d}} \Theta\left[E - \epsilon^j + t^j \cos(k_z d)\right] \mathrm{d}k_{\perp} \ . \tag{2.17}$$

The step function arises from the δ function since its integral is one when the integration interval contains the value zero. In order to perform the last step, some more considerations are needed: it is possible to separate the integration in three energy regions

- $E < \epsilon^j - |t^j|$: the argument of the step DOS is negative, so the function is always zero in the minizone;
- $E > \epsilon^j + |t^j|$: the argument of the step integral is positive and the function is equal to 1;
- $\epsilon^j - |t^j| \leq E \leq \epsilon^j + |t^j|$: the argument of the step function is positive only in an interval between two points symmetric with respect to the center of the minizone.

With these considerations

$$\mathrm{DOS}_j(E) = \frac{V\sqrt{m_x^j m_y^j}}{\pi^2\hbar^2} \begin{cases} 0 & , E < \epsilon^j - |t^j| \\ \frac{1}{d}\mathrm{acos}\left(\frac{E-\epsilon^j}{|t^j|}\right) & , \epsilon^j - |t^j| \leq E \leq \epsilon^j + |t^j| \\ \frac{\pi}{d} & , E > \epsilon^j + |t^j \alpha| \end{cases} \tag{2.18}$$

Now, we use, as a first approximation in the scheme of optical phonon confinement (sec.1.5), the values of M calculated for bulk materials [43]. These matrix elements are directly derived by inserting into the Fermi golden rule the interaction Hamiltonian (eq.1.38 and eq.1.39). For deformation-potential optical phonons we get

$$|M_{\alpha,\beta}(\mathbf{q})|^2 = \frac{\hbar(D_t K)^2}{2\rho V \omega_{op}} \begin{bmatrix} N_{op} \\ N_{op}+1 \end{bmatrix} \ , \tag{2.19}$$

while for polar optical phonons

$$|M_{\alpha\beta}(\mathbf{q})|^2 = \frac{2\pi e^2 E_{op}}{V_0} \frac{\mathbf{q}^2}{(\mathbf{q}^2 - \mathbf{q}_D^2)^2} \left(\frac{1}{\epsilon_+} - \frac{1}{\epsilon_-} \right) \begin{bmatrix} N_{op} \\ N_{op}+1 \end{bmatrix} . \tag{2.20}$$

This last matrix element depends on the transferred wave vector $\mathbf{q}$, and we should not have taken it out of the integration in eq.(2.12). However, we can use the internal rejection tecnique [44] and use the value of $\mathbf{q}$ where M is maximum. The value $\bar{M}$ of the matrix element obtained in this way, is used in the above calculation. In a second moment, once chosen the final scattering state, it is possible to calculate the real scattering probability with $M(\mathbf{k}, \mathbf{k}')$ and to decide if the scattering event is to be considered a real scattering, or a fictitious self-scattering due to the modified probability obtained with $\bar{M}$. In case of a self-scattering, the final state will be equal to the initial one (for details about the Monte Carlo method see app.A).

Using this model for the electron-phonon interaction, the scattering probability for the phonon modes used in the simulation are shown in Fig.2.1 Fig.2.2 Fig.2.3. The step-like shape derives directly from the integration of the delta function and rensembles the density of states of the superlattice. The polar optical phonon scattering probability has been represented using the maximized matrix element $\bar{M}$.

2.2.1 Using the scattering probability

In order to understand how the interaction with phonons is treated in the Monte Carlo simulator, some considerations have to be pointed out. First of all we know that block states (i.e. the envelope function in our case) are extended all over the superlattice. Also the phonon wave function are, in general, extended all over the system, and the matrix element $M(\mathbf{k}, \mathbf{k}')$ is calculated by integrating over the whole space, like in a bulk lattice. On the other hand, superlattice phonon modes, as said before, are confined [38],

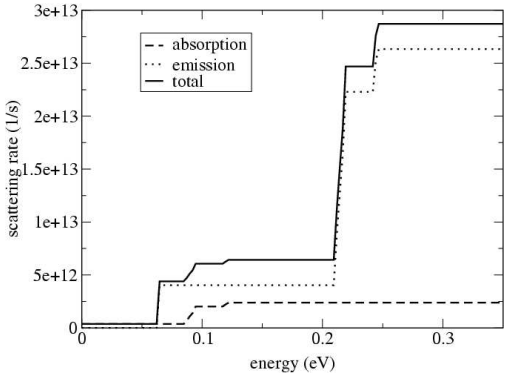

Figure 2.1: *Optical phonon scattering rate for silicon layer. The step shape of the probability arises from the DOS of the superlattice.*

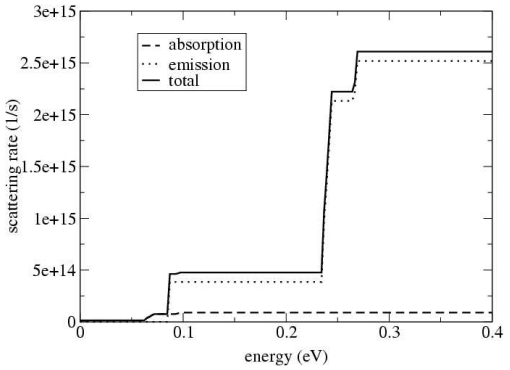

Figure 2.2: *Polar optical phonon scattering rate for silicon dioxide. This is the maximized probability obtained before using the rejection tecnique.*

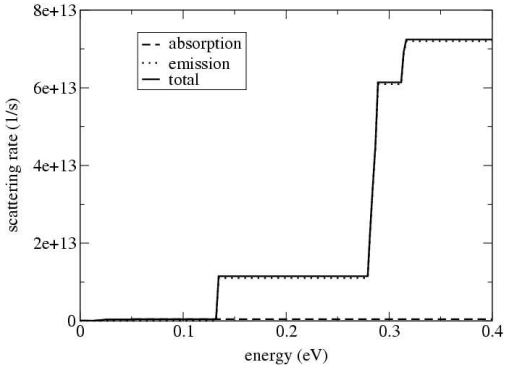

Figure 2.3: *Deformation potential optical phonon scattering rate in silicon dioxide.*

that is the phonon wave function is composed of two parts: if we consider, for example, silicon phonon mode, the wave function is oscillating in the silicon slab and it is evanescent in the oxide slab. Moreover, when using a Monte Carlo approach for the study of transport, the simulated electron is localized in space. This means that when we consider the electron phonon interaction in the numerical code, we can use the matrix element calculated for the bulk interaction, but we give the electron the possibility to interact only with the phonon modes of the material it is localized in. This approximation is reasonable also considering the fact that the optical phonon group velocity is zero.

2.3 Results

The theory described above has been applied to the superlattice under investigation. A monte Carlo code has been written in order to perform transport calculation (as described in appendix A), where we have collected, in particular, drift velocity, mean energy, energy and momentum distribution function. Moreover, in the calculation, the position of the simulative electron is taken into account in order to include the right scattering mechanisms as explained above.

2.3.1 Distribution functions

The first results presented in this chapter are the distribution functions for energy and momentum. The distribution functions are important in order to understand the drift velocity and mean energy behavior. The distribution of electrons in lowest miniband as function of the vertical component of the momentum k_z is reported in Fig.2.4, at three different values of electric field. We can see that at low fields, the distribution is almost symmetric, at intermediate fields the maximum shifts toward band regions where the

group velocity is higher, at higher fields the distribution is nearly flat, thus negative k_z points reduce the drift velocity. Moreover the variation between the minimum and the maximum value of the distribution is very low at all fields. This variation is the cause of the small net positive drift velocity along the z direction, and, at higher electric fields, the nearly flat distribution gives a very low contribution to the drift velocity.

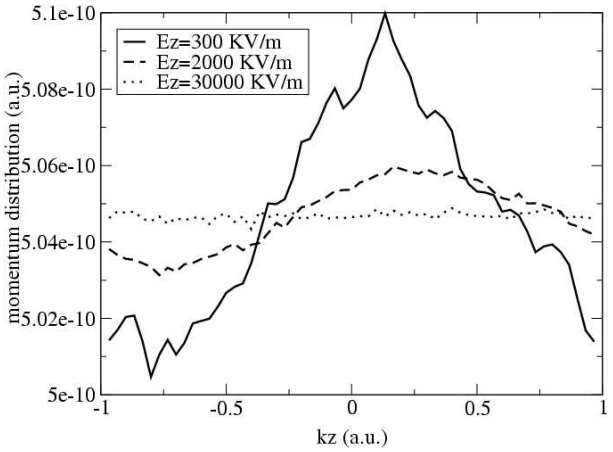

Figure 2.4: *Momentum distribution function for the k_z direction, for the lowest miniband.*

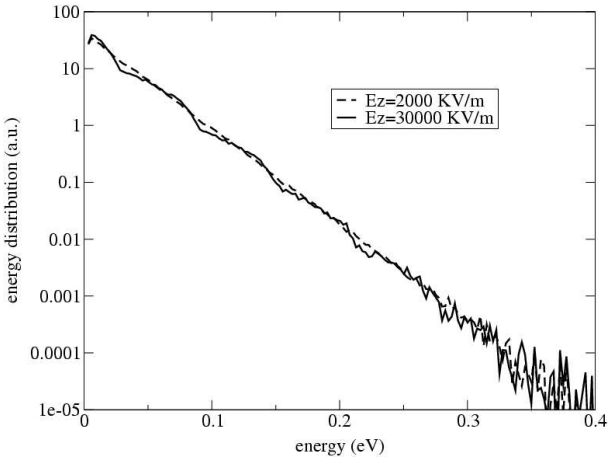

Figure 2.5: *Energy distribution function for the first miniband, at two different electric fields.*

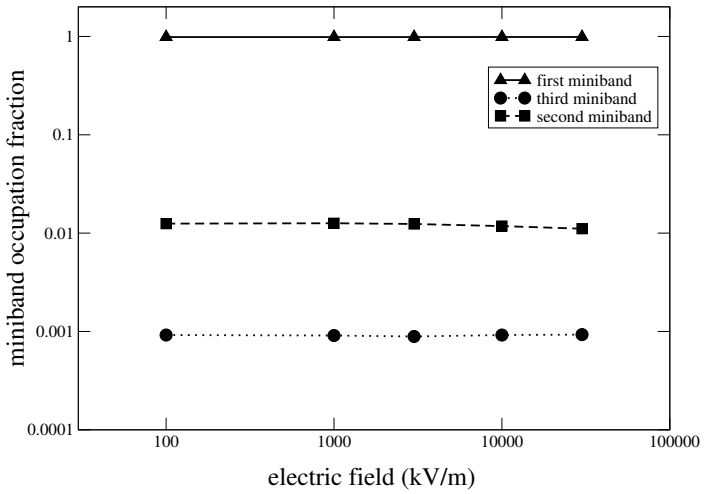

Figure 2.6: *Population of the minibands.*

The energy distribution function is shown in Fig.2.5. It can be seen that at low electric field electrons are termally distributed with a mean energy $\bar{E} = 26.1$ meV, as predicted from the calculations (see app.B.2). At high electric fields, the distribution function does not show any heating of the carriers and assumes an undulated shape due to the interplay between phonon energies and energy distance between wells: the scattering depletes the distribution function near the 90 meV region (corresponding to the energy of the polar optical phonon), the the other undulations are replicas of the first one. The narrow miniband shape prevents a rpaid thermalization. Probably, the introduction of a low energy scattering mechanism, such as acoustic phonon scattering, would avoid this high field effect.

At last, the miniband occupation, is represented in Fig.2.6, for different applied fields. The electric field does not influence the population in the three minibands as effect of the absent heating of the distribution.

2.3.2 Negative differential conductivity

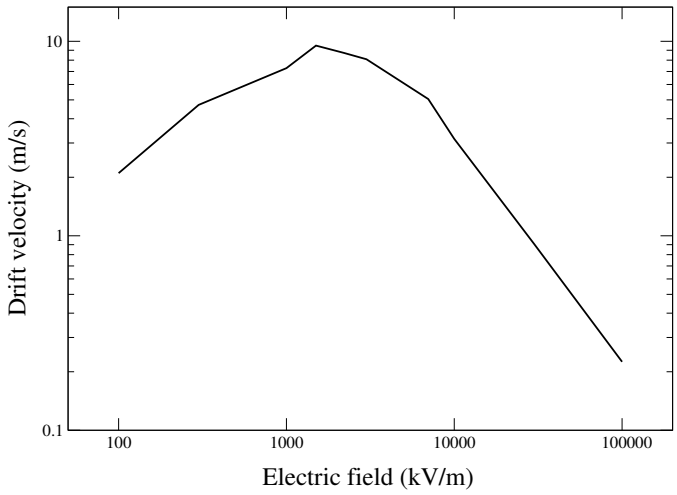

Figure 2.7: *Drift velocity.*

The drift velocity (Fig.2.7) is in general very low, of the order of 10 m/s, as anticipated, since the miniband is very narrow and the momentum distribution function is nearly omogeneous in the minizone. The maximum velocity is obtaind at electric field of about 2000 kV/m. At higher fields the negative differential conductivity (NDC) behavior, as predicted by the Esaki-Tsu model [42] is observed. The the NDC is explained in terms of the momentum distribution function (Fig.2.4): in general the drift velocity in each miniband can be written as

$$v_d(z) = \int_{BZ} \mathrm{d}k_z v_g(k_z) f(k_z) \tag{2.21}$$

and it is easy to understand that at low fields the drift velocity increases with the electric field, since the predominant behavior of the distribution is the right-shift of the maximum, but at higher fields the distribution slowly flattens to a constant value and the drift velocity decreases.

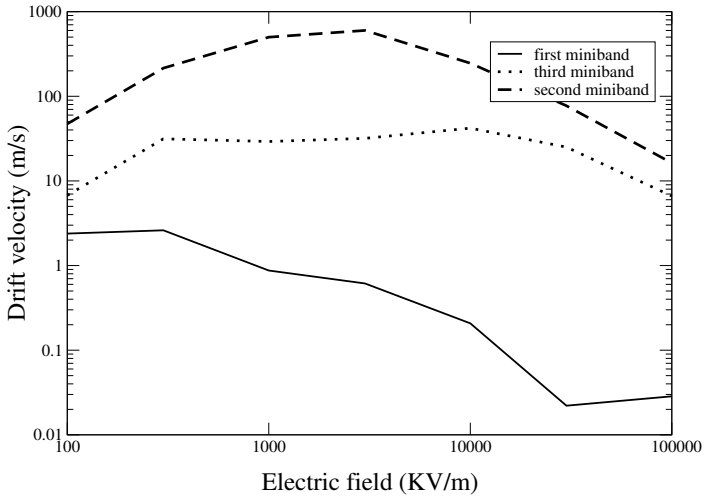

Figure 2.8: *Drift velocity in each miniband: the contribution of the miniband to the total drift velocity can be obtained by multiplying this curves with the corresponding occupation fraction.*

It can be seen that, although the miniband occupation is constant at different electric fields, the overall drift velocity curve is divided into two regions in which different minibands dominate the transport properties (Fig.2.8). In particular in the first region ($F < 1000$ kV/m) behavior is dominated by the first miniband, while the second miniband velocity dominte the complementary region. This is because the second miniband, which is less flat than the first one, is charachterized by higher drift velocity and the maximum is located at higher fields, but, since it is less populated, its contribution is comparable only at fields higher than 1000 kV/m.

2.3.3 Mean energy

As regards the mean energy, it can be seen that a decrease in mean energy, of about 1 meV occurs at high electric field. Looking at the distribution

function of Fig.2.5, for $E_z = 2000$ kV/m the electron kinetic energy is 26.1 meV, while the second distribution corresponds to an energy value of 25.3 meV. This behavior is caused by the particular shape of the distribution function: since the phonon slightly depletes a particular energy region, the effect is a little reduction of the mean electron energy. This effect should be probably removed with the introduction of a mechanism able to exchange small amount of energy with the electrons. It has been shown [45] that in a different superlattice, with wider minibands, the mean energy increases of the order of the miniband width, owing to the shift of the momentum distribution function toward high enery regions. The oscillating shape of the distribution function doesn't appear in this case because the distribution is smeared by the small amount of energy needed is given by the electric field along the miniband.

Chapter 3

Oblique transport in Si/SiO_2 superlattices

3.1 Effects of a parallel (inplane) electric field

When the electric field is applied along the vertical direction z of a superlattice, the carrier drift velocity shows the negative differential conductivity behavior, and the absolute value of the drift velocity is very low, as seen in the previous chapter, owing to the very flat shape of the miniband.

A parallel field component has been added to the vertical field, in order to investigate the influence of a parallel electric field, on vertical transport. The field component along the plane is varied from 0 to 1200 kV/m, while the vertical component is constant at 2000 kV/m, which is the value of the maximum drift velocity in the vertical simulation (see previous chapter).

3.2 Results

Since the electron mass is anisotropic, the electron mobility is much higher along the in plane direction, about three or four orders of magnitude higher

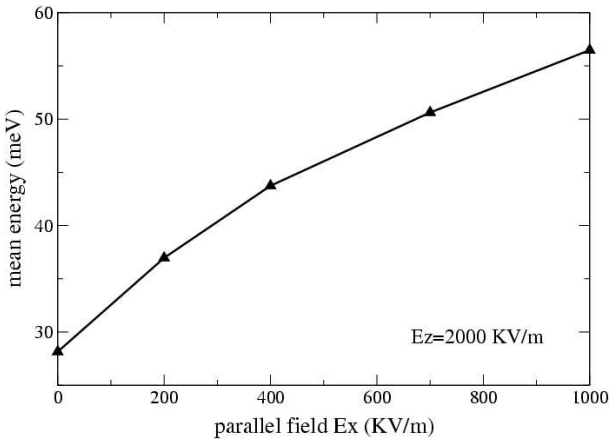

Figure 3.1: *Mean kinetic energy as functions of the parallel field with constant field along z direction, for a 24/7.68 Å Si/SiO_2 SL.*

then along the vertical direction: the resulting drift velocity is not parallel to the electric field. A typical result with $E_z = 3000\,\mathrm{KV/m}$ and $E_x = 200\,\mathrm{KV/m}$ is a drift velocity of $v_{d,z} = 6.5$ m/s and $v_{d,x} = 60000$ m/s. In the following subsections vertical drift velocity v_z, mean energy and their dependences upon parallel electric field are investigated.

3.2.1 Mean energy

First of all, we analyse the mean energy (Fig.3.1). It can be seen that a strong heating of the electrons occurs when a parallel field is added to the vertical component. Mean energy increases almost linearly and reaches a value, in our electric field range, of 57 meV, that is more than double than the termal energy. This heating can be observed looking at the energy distribution function (Fig.3.2). The distribution deviates from the perfect esponential shape and regions with different slopes appear in the exponential plot. This behavior is strongly dependent on the phonon scattering rate: at low energy, electrons have little possibility to dissipate and they heat up to temperature higher than equilibrium. When the energy is high enough to allow phonon emis-

sion, the termalization is more efficient and the distribution slope changes. Each kink in the distribution corresponds to a phonon emission step, as can be deduced from the comparison between the distribution function and the

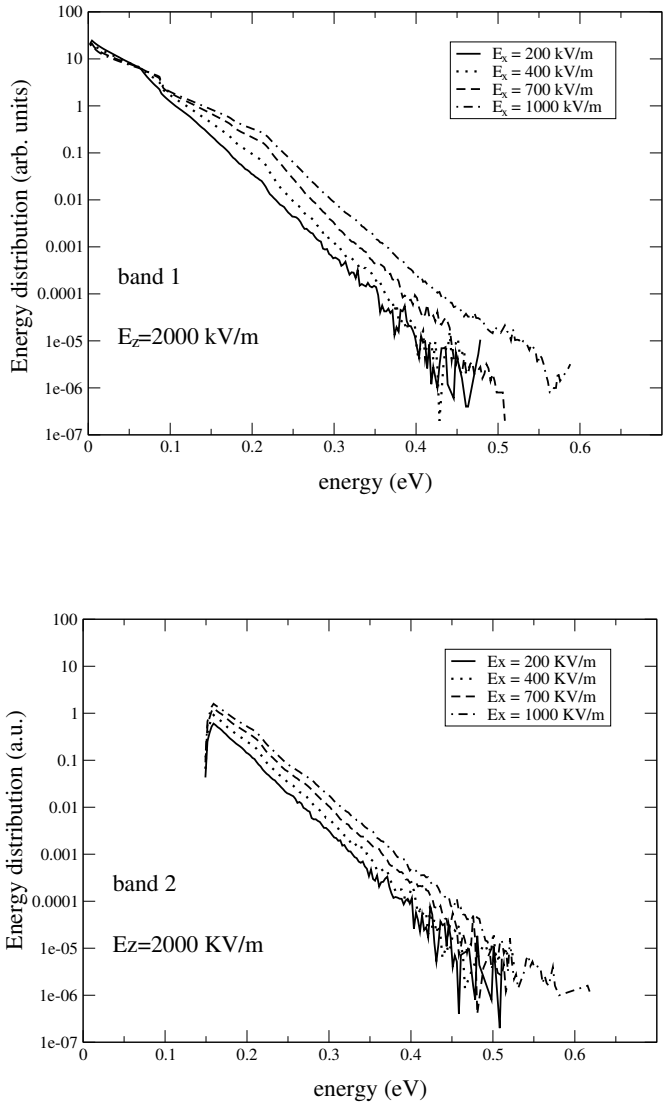

Figure 3.2: *Energy distribution function, in the first miniband and the second miniband, for several values of parallel electric field E_x.*

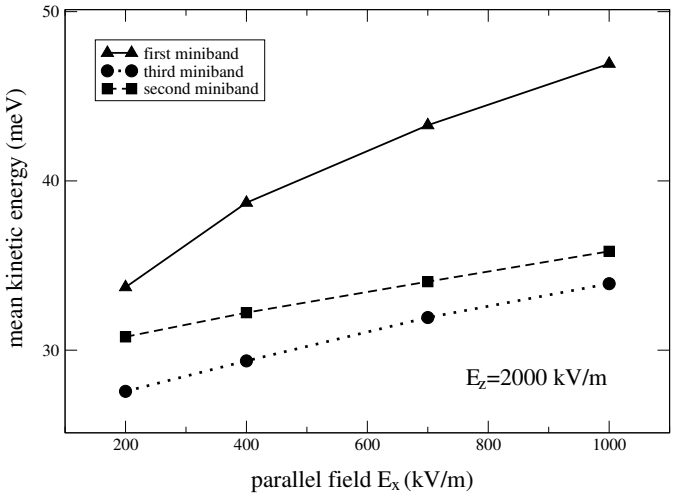

Figure 3.3: *Mean energy, above the bottom of each miniband, in a 24/7.7 Å Si/SiO_2 SL.*

scattering rates of section 2.2.

Another consideration can be deduced looking at the mean electron kinetic energy in each miniband (Fig.3.3): the strongest energy increase concerns the first miniband since in this band the scattering rate is lower.

What happens is that the parallel electric field heats the electrons along the parabolic direction of the bands and the scattering mechanisms redistribute the energy along all three directions. As seen before, the interband scattering is a very important mechanism at this transport regime, thus it can be deduced that the population of electrons in minibands higher than the first one, will increase considerably owing to the electron heating. The miniband occupation as a function of the paralle component of the electric field has been studied and results are shown in Fig.3.4: the number of electrons in the higher bands is very low if compared to the one of the first band, but it increases when the parallel field is added, owing to the parallel heating. This population change will strongly affect also the drift velocity along

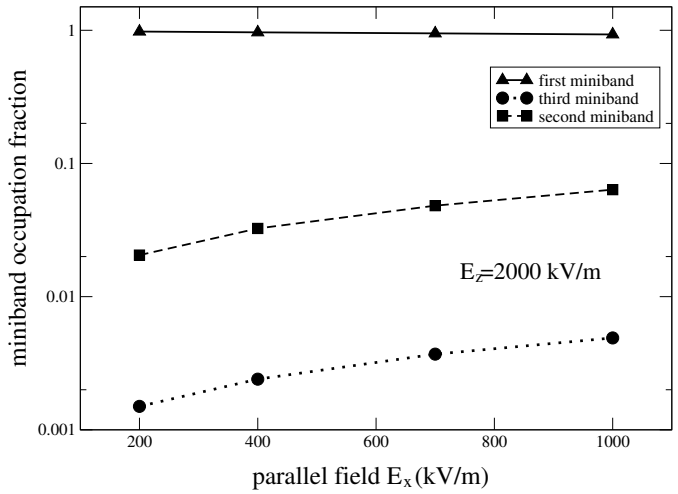

Figure 3.4: *Population fraction for a 24/7.68 Å Si/SiO_2 SL.*

the vertical direction, as described in the following section: the properties of the higher minibands will became more and more important increasing the parallel field.

3.2.2 Drift velocity

The principal effect of the parallel component of the electric field is a strong increase of the drift velocity (Fig.3.5). When a lateral field of 1000 kV/m is applied, electrons move about three times faster than with only vertical field applied. First of all, the population change in the different minibands is sufficient to explain this effect: since different minibands contribute with different values to the total drift velocity (as seen in vertical field simulations, see for example Fig.2.8), the increase of population in higher minibands will change the weight of these contributions and, in this way, "faster" minibands give a more important contribution to transport. A second reason exists, however, for this strong improvement: the drift velocity is enhanced in each

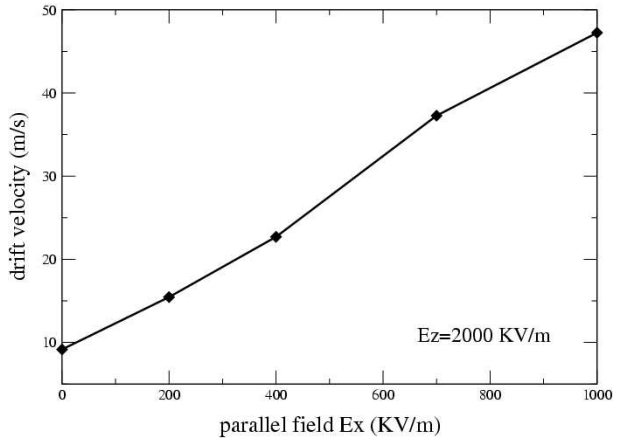

Figure 3.5: *Drift velocity as function of the parallel field with constant field along z direction, for a 24/7.68 Å Si/SiO_2 SL.*

miniband separately as can be seen from the saparated curves in Fig.3.6. This phenomenon is confirmed by the momentum distribution functions in the minibands (Fig.3.7). The application of the parallel electric field depletes the negative group velocity regions and favors the positive group velocity with

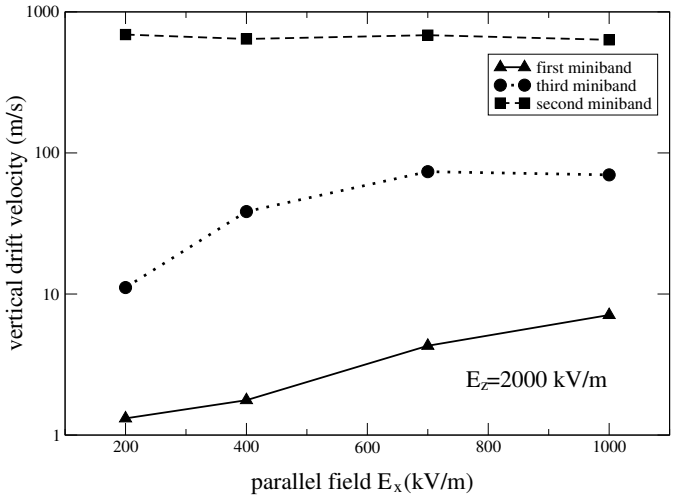

Figure 3.6: *Drift velocity for each miniband in a 24/7.68 Å Si/SiO_2 SL.*

a global enhancement of the drift velocity for electrons in the miniband. This effect is the opposite of what seen in the previous chapter where the vertical field flatten the momentum distribution function and for highr fields the result is a decrease of the drift velocity.

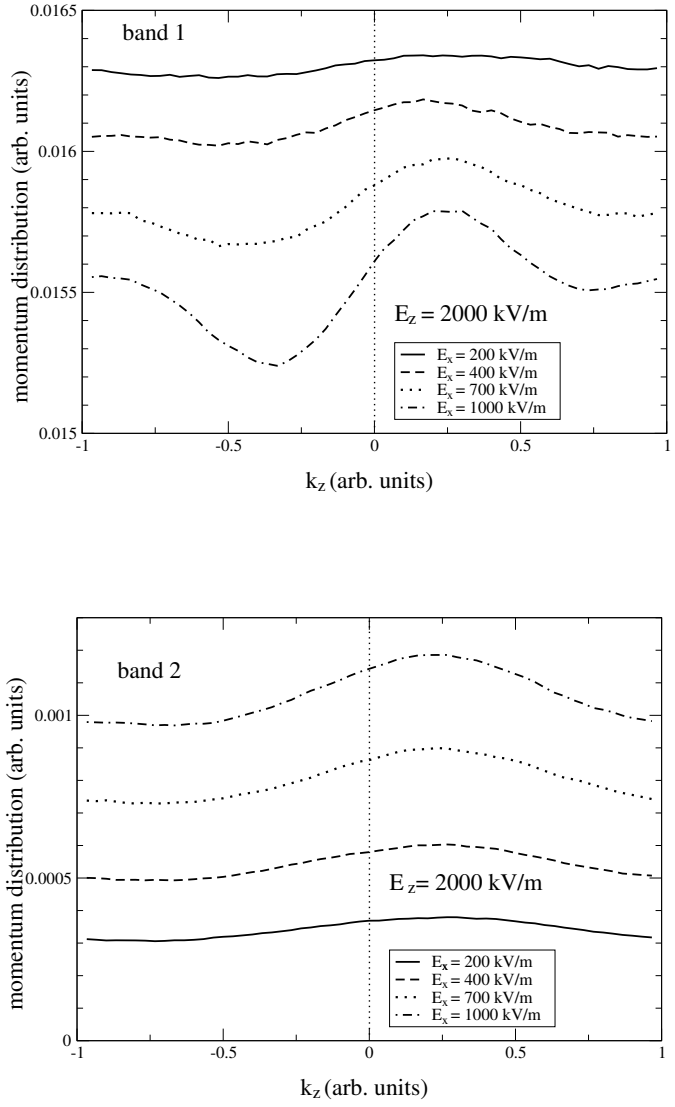

Figure 3.7: *Momentum distribution function, in the miniband 1 and 2, for several values of parallel electric field E_x.*

Chapter 4

Wannier-Stark formulation of transport

4.1 Motivation

The Monte-Carlo simulation used in the previous chapters, is based on the semiclassical approximation for the electron motion. The miniband transport description is useful when the miniband width is greater than the voltage drop over a SL period i.e. $eEd < 2\tilde{t}$; beyond this limit, a quantum description is required [46]. The first miniband (that is less than 1 meV wide) satisfies this condition for fields lower than 200 KV/m. The second miniband is about 9 meV wide and satisfies the former condition when $E_z < 3000$ KV/m. Since in the diagonal simulations a vertical field $E_z = 2000$ KV/m is used, the semiclassical model should be applicable. for rlectrons in the second miniband. However also at high fields the population, as seen in Fig.2.6, is almost all in the first miniband, thus a quantum theory of transport is required; in particular such a theory should avoid any use of classical dynamics.

The description chosen for further calculation is based on the formalism of the Wannier-Stark function. These functions are eigenstates of the su-

perlattice Hamiltonian, including the electric field, and, in principle, should be able to give rise to more accurate results than in the semiclassical case, especially at high fields. In particular, the drift velocity curve will show features absent in the semiclassical case owing to the particular interaction of the electronic states with phonons.

4.2 Wannier-Stark functions

The Schrödinger equation to solve now is the following

$$\widehat{H}_0\Psi - eFz\Psi = \epsilon\Psi \tag{4.1}$$

where we have used the crystal hamiltonian in the envelope-function and parabolic-band approximations

$$\widehat{H}_0 = \frac{\widehat{\mathbf{p}}^2}{2m^*} + \widehat{V}(\mathbf{r}) \ .$$

Now, let us use, for simplicity, the Dirac notation, so we write $|\Psi\rangle$ for the wave vector, $\Psi(x) = \langle x|\Psi\rangle$, and the above equation is

$$\widehat{H}_0|\Psi\rangle - eFz|\Psi\rangle = \epsilon|\Psi\rangle \ . \tag{4.2}$$

We can now expand the solution over the superlattice bloch states $|n,k\rangle$, eigenstates of the Hamiltonian $\widehat{H}_0$

$$|\Psi\rangle = \sum_{n'} \int_{\mathbf{k}'} \mathrm{d}\mathbf{k}' \langle \mathbf{k}'n'|\Psi\rangle |\mathbf{k}'n'\rangle \tag{4.3}$$

and substitute it to the above Schrödinger equation; multiplying by $\langle \mathbf{k}n|$ it follows that

$$\sum_{n'} \int_{\mathbf{k}'} \mathrm{d}\mathbf{k}' \langle \mathbf{k}n|\widehat{H}_0|\mathbf{k}'n'\rangle\langle \mathbf{k}'n'|\Psi\rangle - eF \sum_{n'} \int_{\mathbf{k}'} \mathrm{d}\mathbf{k}' \langle \mathbf{k}n|z|\mathbf{k}'n'\rangle\langle \mathbf{k}'n'|\Psi\rangle +$$
$$- \sum_{n'} \int_{\mathbf{k}'} \mathrm{d}\mathbf{k}' \epsilon \langle \mathbf{k}n|\mathbf{k}'n'\rangle\langle \mathbf{k}'n'|\Psi\rangle$$

$$
\begin{aligned}
&= \sum_{n'} \int_{\mathbf{k}'} \mathrm{d}\mathbf{k}' \, (E_n(\mathbf{k}) - \epsilon) \, \delta_{n'n} \delta(\mathbf{k}' - \mathbf{k}) \langle \mathbf{k}' n' | \Psi \rangle \\
&\quad -eF \sum_{n'} \int_{\mathbf{k}'} \mathrm{d}\mathbf{k}' \langle \mathbf{k} n | z | \mathbf{k}' n' \rangle \langle \mathbf{k}' n' | \Psi \rangle \\
&= (E_n(\mathbf{k}) - \epsilon) \, \langle \mathbf{k} n | \Psi \rangle - eF \sum_{n'} \int_{\mathbf{k}'} \mathrm{d}\mathbf{k}' \langle \mathbf{k} n | z | \mathbf{k}' n' \rangle \langle \mathbf{k}' n' | \Psi \rangle \ . \qquad (4.4)
\end{aligned}
$$

Since the system is separable, it is convenient to take into account only the one-dimensional problem along the electric field direction z. In particular, the following calculation is performed using the real space representation:

$$
\begin{aligned}
\phi_{nk_z}(z) &= \langle k_z n | \Psi \rangle \\
\psi_{nk_z} &= \langle z | k_z n \rangle = u_{nk_z}(z) e^{ik_z z} \\
\Psi &= \sum_n \int_{k_z} \mathrm{d}k_z \phi_n(k_z) \psi_{nk_z}(z) \ . \qquad (4.5)
\end{aligned}
$$

The value $\langle \mathbf{k} n | z | \mathbf{k}' n' \rangle$ has to be calculated explicitely:

$$
\begin{aligned}
\langle \mathbf{k} n | z | \mathbf{k}' n' \rangle &= \int \mathrm{d}z e^{i(k'_z - k_z)z} u^*_{nk_z}(z) z u_{n'k'_z}(z) \\
&= \frac{1}{i} \frac{\mathrm{d}}{\mathrm{d}k_z} \int \mathrm{d}z e^{i(k'_z - k_z)z} u^*_{nk_z}(z) u_{n'k'_z}(z) \\
&\quad -\frac{1}{i} \int \mathrm{d}z e^{i(k'_z - k_z)z} u^*_{nk_z}(z) \frac{\mathrm{d}}{\mathrm{d}k'_z} u_{n'k'_z}(z) \qquad (4.6)
\end{aligned}
$$

Since the first term is the scalar product of two Bloch functions, the result is a Dirac delta; in the second term there is a periodic function ($u^* \frac{\mathrm{d}}{\mathrm{d}k'_z} u$) of the position. As a result, the second integral is proportional to the momenum Dirac delta

$$
\langle \mathbf{k} n | z | \mathbf{k}' n' \rangle = \frac{1}{i} \frac{\mathrm{d}}{\mathrm{d}k'_z} \delta_{nn'} \delta(k_z - k'_z) + X_{nn'} \delta(k_z - k'_z) \qquad (4.7)
$$

where

$$
X_{nn'} = \frac{2\pi i}{L} \int \mathrm{d}z u^*_{nk_z}(z) \frac{\mathrm{d}}{\mathrm{d}k'_z} u_{n'k_z}(z) \ .
$$

It is convenient to consider a one-band model for the calculation, and then we can neglect off-diagonal terms in this last term. By defining

$$
E^{(1)}_n(k_z) = E_n(k_z) - eEX_{nn} \qquad (4.8)
$$

we obtain the final expression for the one-dimensional Schrödinger equation in k representation

$$\left[E_n^{(1)}(z) - ieF\frac{\mathrm{d}}{\mathrm{d}k_z}\right]\phi_n(k_z) = \epsilon\phi_n(k_z)\ . \tag{4.9}$$

The solution follows from immediate integration of this equation

$$\phi_n(k_z) = ce^{\frac{i}{eF}\int_0^{k_z}\mathrm{d}k'_z[E-E_n^{(1)}(k'_z)]}\ , \tag{4.10}$$

where c is a normalization constant. The energy eigenvalues can be obtained from the boundary condition: the function must satisfy $\phi(-\frac{\pi}{L}) = \phi(\frac{\pi}{L})$ since the two Brillouin zone boundaries are the same k point. From that condition follows that

$$\frac{1}{eF}\int_{-\frac{\pi}{L}}^{\frac{\pi}{L}}\mathrm{d}k'_z\left[E^\nu - E_n^{(1)}(k'_z)\right] = 2\nu\pi \tag{4.11}$$

$$E^\nu = \nu eFL + \frac{L}{2\pi}\int_{-\frac{\pi}{L}}^{\frac{\pi}{L}}\mathrm{d}k'_z E_n^{(1)}(k'_z)\ . \tag{4.12}$$

This means that an infinite set of equally spaced energy levels arise from the band of the unbiased superlattice. These levels are spaced of a value eFL and are designated as Wannier levels, or Wannier-Stark (WS) ladder. The Wannier-Stark function are mostly localized in a single well, and the localization increases with the electric field. The WS state is in close relationship with the Bloch oscillation described in section 2.1, in fact the spatial extension of the oscillation is comparable to the localization of the WS state. Moreover, the energy separation between the WS states is $\Delta E = \hbar\omega$, with ω the frequency of the bloch oscillation.

The exixtence of the Wannier-Stark ladder has been quite controversial, until their the experimental observation, reported in 1988 [47].

Along the two other lattice directions, the Hamiltonian describes a free particle motion, then the wave eigenfunctions will be plane waves with parabolic energy dispersion. The total wave function, in real three-dimensional space,

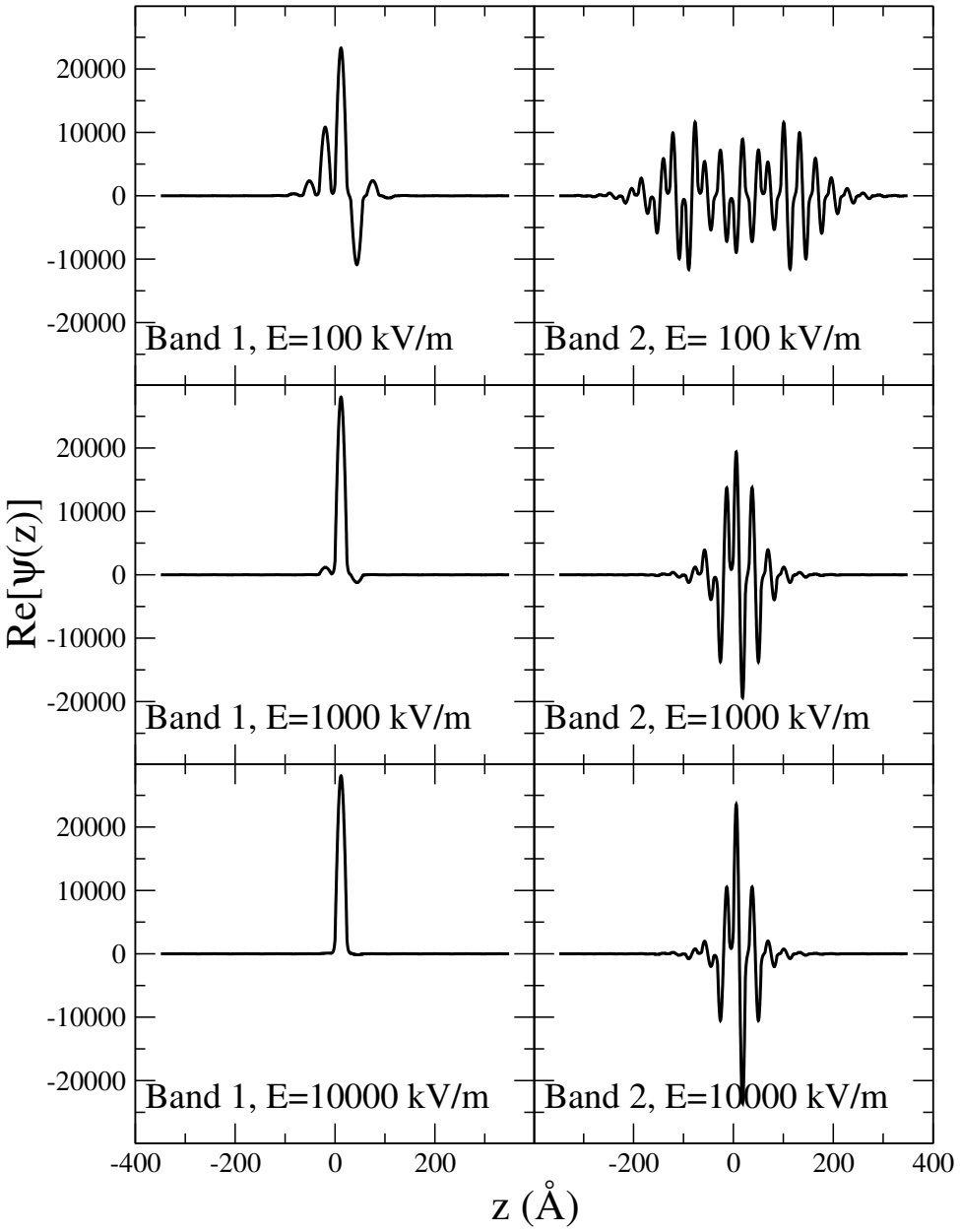

Figure 4.1: *Wannier-Stark functions (real part) calculated for our system at different electric fields for the first and the second level. These functions are more localized when the electric field is high and first-level sunctions are more localized than the second-level ones.*

results to be

$$\Psi^{\nu}_{n\mathbf{k}}(\mathbf{r}) = ce^{ik_x x}e^{ik_y y}\int_{-\frac{\pi}{L}}^{\frac{\pi}{L}} \mathrm{d}k_z \psi_{nk_z}(z) e^{\frac{i}{eF}\int_0^{k_z}\mathrm{d}k'_z[E^{\nu}-E^{(1)}_n(k'_z)]} \ , \tag{4.13}$$

and the energy eigenvalues are

$$E^{\nu}_n(k_x,k_y) = \nu eFL + \frac{L}{2\pi}\int_{-\frac{\pi}{L}}^{\frac{\pi}{L}} \mathrm{d}k'_z E^{(1)}_n(k'_z) + \frac{\hbar^2}{2m_x}k_x^2 + \frac{\hbar^2}{2m_y}k_y^2 \ . \tag{4.14}$$

The Wannier-Stark functions, calculated for the system under investigation, are represented in Fig.4.1. The WS eigenstates used in the following derives from Block states and minibands calculated using the Krönig-Penney potential for the z direction of the superlattice.

4.2.1 Properties of the WS functions

Now we will analyse in more detail some properties of the Wannier-Stark functions:

- The functions are more localized when the electric field is high (as can be seen in Fig4.1). This is compatible with the Bloch oscillation picture described before. In particular, in the limit of zero field ($F \to 0$) it can be seen that the WS functions tend to Bloch states.

- $\Psi^{\nu}(z) = \Psi^0(z-\nu L)$, in fact we can write, using expression (4.12):

$$\Psi^{\nu}(z) = c\int_{-\frac{\pi}{L}}^{\frac{\pi}{L}} \mathrm{d}k_z \psi_{k_z}(z) e^{\frac{i}{eF}\int_0^{k_z}\mathrm{d}k'_z[E_0+\nu eFL-E^{(1)}_n(k'_z)]} \tag{4.15}$$

  with $E_0 = \frac{L}{2\pi}\int_{-\frac{\pi}{L}}^{\frac{\pi}{L}} \mathrm{d}k'_z E^{(1)}(k'_z)$. Using now the equations (4.5), (4.10) and the Bloch Theorem we can write

$$\begin{aligned}
\Psi^{\nu}(z) &= \int_{-\frac{\pi}{L}}^{\frac{\pi}{L}} \mathrm{d}k_z \phi_0(k_z) e^{ik_z\nu L}\psi_{k_z}(z) \\
&= \int_{-\frac{\pi}{L}}^{\frac{\pi}{L}} \mathrm{d}k_z \phi_0(k_z)\psi_{k_z}(z-\nu L) \\
&= \Psi^0(z-\nu L)
\end{aligned} \tag{4.16}$$

- From the figure we can see that the first level WS function is much more localized than the second level one since the former is chacterized by a lower energy. Moreover, the first level function presents one oscillation per well, while the seconfunction shows two oscillations.

4.3 Transition probabilities

In order to study the interaction of the carriers with the crystal, we consider, in the following, the system composed by the electron and the phonon gas. The transition probabilities used in the Wannier-Stark transport model, have been calculated starting from the Fermi Golden rule. We now indicate the eigenstates of the system as $|\nu n\mathbf{k}, n_{\mathbf{q}}\rangle$ where ν is the number of the well, n is the band index, $\mathbf{k}$ is the two-dimensional wave vector in the parallel direction and $n_{\mathbf{q}}$ is the phonon occupation. Now the Fermi rule can be written as

$$\begin{aligned} P(\nu n\mathbf{k}n_{\mathbf{q}}, \nu' n'\mathbf{k}' n_{\mathbf{q}'}) &= \frac{2\pi}{\hbar}\sum_{\mathbf{q}} \left|\langle \nu' n'\mathbf{k}', n'_{\mathbf{q}}|\widehat{H}_{e-ph}(\mathbf{q})|\nu n\mathbf{k}, n_{\mathbf{q}}\rangle\right|^2 \times \\ &\quad \delta\left[\epsilon(n\mathbf{k}) - \epsilon(n'\mathbf{k}') \mp \hbar\omega_{op} + \nu eFd\right] \ , \end{aligned} \tag{4.17}$$

where $\widehat{H}_{e-ph}(\mathbf{q})$ is the electron-phonon interaction Hamiltonian of eq.(1.37). As a first step to the calculation of the matrix element of the interaction hamiltonian, we write the wave function as the product of lattice and electronic wave functions

$$|\nu n\mathbf{k}, n_{\mathbf{q}}\rangle = |n_{\mathbf{q}}\rangle|\nu n\mathbf{k}\rangle = |n_{\mathbf{q}}\rangle|\nu n\rangle|\mathbf{k}\rangle \ , \tag{4.18}$$

so that the calculation is developed as follows

$$\begin{aligned} & \langle \nu' n'\mathbf{k}'|\langle n'_{\mathbf{q}}|c(\mathbf{q})\left(a_{\mathbf{q}}e^{i\mathbf{qr}} + a^{\dagger}_{\mathbf{q}}e^{-i\mathbf{qr}}\right)|n_{\mathbf{q}}\rangle|\nu n\mathbf{k}\rangle = \\ = \ & c(\mathbf{q})\langle \nu' n'\mathbf{k}'|\langle n'_{\mathbf{q}}|a_{\mathbf{q}}e^{i\mathbf{qr}}|n_{\mathbf{q}}\rangle|\nu n\mathbf{k}\rangle + c(\mathbf{q})\langle \nu' n'\mathbf{k}'|\langle n'_{\mathbf{q}}|a^{\dagger}_{\mathbf{q}}e^{-i\mathbf{qr}}|n_{\mathbf{q}}\rangle|\nu n\mathbf{k}\rangle \\ = \ & c(\mathbf{q})\sqrt{n_{\mathbf{q}}}\langle \nu' n'\mathbf{k}'|e^{i\mathbf{qr}}|\nu n\mathbf{k}\rangle\delta_{n_{\mathbf{q}},n_{\mathbf{q}-1}} \\ & + c(\mathbf{q})\sqrt{n_{\mathbf{q}}+1}\langle \nu' n'\mathbf{k}'|e^{-i\mathbf{qr}}|\nu n\mathbf{k}\rangle\delta_{n_{\mathbf{q}},n_{\mathbf{q}}+1} \ , \end{aligned} \tag{4.19}$$

and the exponential term can be calculated explicitely

$$\begin{aligned}\langle \nu' n' \mathbf{k}' | e^{\mp i \mathbf{q} \mathbf{r}} | \nu n \mathbf{k} \rangle &= \langle \nu' n' | e^{\mp i q_z z} | \nu n \rangle \langle \mathbf{k}' | e^{\mp i \mathbf{q}_{\|} \mathbf{r}_{\|}} | \mathbf{k} \rangle \\ &= \delta_{\mathbf{k}-\mathbf{k}' \mp \mathbf{q}_{\|}} \langle \nu' n' | e^{\mp i q_z z} | \nu n \rangle \ . \end{aligned} \tag{4.20}$$

Finally, the transition probability for the electrons, according to the first order perturbation theory is

$$\begin{aligned} P(\nu n \mathbf{k}, \nu' n' \mathbf{k}') &= \frac{2\pi}{\hbar} \sum_{\mathbf{q}} c^2(\mathbf{q}) \begin{bmatrix} n_{\mathbf{q}} \\ n_{\mathbf{q}} + 1 \end{bmatrix} \left| \langle \nu' n' | e^{\mp i q_z z} | \nu n \rangle \right|^2 \times \\ & \delta_{\mathbf{k}-\mathbf{k}' \mp \mathbf{q}_{\|}} \delta \left[\epsilon(n\mathbf{k}) - \epsilon(n'\mathbf{k}') \mp \hbar\omega_{op} + \nu e F d \right] \end{aligned} \tag{4.21}$$

where $n_{\mathbf{q}}$ is the mean value of the phonon occupation. We are interested in the total scattering probability from a state $(\nu n \mathbf{k})$ to any possible final state $\mathbf{k}'$. We integrate over the momentum variable, but we not perform the sum over $\nu' n'$, since it is useful to keep separate these probabilities in order to easily determine the final state after scattering. The momentum conservation delta function is then used to eliminate the integration over $\mathbf{q}_{\|}$, which becomes now $\mathbf{q}_{\|} = \mathbf{k}' - \mathbf{k}$. Moreover, the tranformation into elliptical coordinates is useful

$$\begin{cases} k'_x &= \sqrt{\frac{m_x}{m_0}} l' \cos\theta \\ k'_y &= \sqrt{\frac{m_y}{m_0}} l' \sin\theta \end{cases} \tag{4.22}$$

and the integral is now

$$\begin{aligned} P_{\nu' n'}(\nu n \mathbf{k}) &= \frac{1}{(2\pi)^5 \hbar} \frac{\sqrt{m_x m_y}}{m_0} \int l' \mathrm{d}l' \int \mathrm{d}\theta \int \mathrm{d}q_z c^2(\mathbf{q}) \begin{bmatrix} n_{\mathbf{q}} \\ n_{\mathbf{q}} + 1 \end{bmatrix} \times \\ & \left| \langle \nu' n' | e^{\mp i q_z z} | \nu n \rangle \right|^2 \delta \left[\epsilon(n\mathbf{k}) - \epsilon(n'\mathbf{k}') \mp \hbar\omega_{op} + \nu e F d \right] \\ &= \frac{\sqrt{m_x m_y}}{(2\pi)^5 \hbar^3} \int \mathrm{d}\epsilon' \int \mathrm{d}\theta \int \mathrm{d}q_z c^2(\mathbf{q}) \begin{bmatrix} n_{\mathbf{q}} \\ n_{\mathbf{q}} + 1 \end{bmatrix} \times \\ & \left| \langle \nu' n' | e^{\mp i q_z z} | \nu n \rangle \right|^2 \delta \left[\epsilon(n\mathbf{k}) - \epsilon' \mp \hbar\omega_{op} + \nu e F d \right] \end{aligned} \tag{4.23}$$

where the substitution $\epsilon' = \epsilon(n'\mathbf{k}') = \frac{\hbar^2 l'^2}{2m_0}$ has been used. Moreover, for optical phonons, $n_{\mathbf{q}}$ is constant for a given temperature and should be put

out of the integration. The energy conservation delta function is now used to eliminate the integration over ϵ', and the final scattering probability is now

$$P_{\nu' n'}(\nu n \mathbf{k}) = \frac{\sqrt{m_x m_y}}{(2\pi)^5 \hbar^3} \left[\begin{array}{c} n \\ n+1 \end{array} \right] \int \mathrm{d}\theta \int \mathrm{d}q_z c^2(\mathbf{q}) \left| \langle \nu' n' | e^{\mp i q_z z} | \nu n \rangle \right|^2 . \tag{4.24}$$

The integrations of the delta functions has introduced the following conditions over the transferred wave vector

$$\mathbf{q} = (k'_x - k_x,\ k'_y - k_y,\ q_z) \tag{4.25}$$

where the wave vector $\mathbf{k}'$ is calculated through the transformation (4.22), and l' is obtained as follows

$$l' = \frac{\sqrt{2 m_0 \epsilon'}}{\hbar}$$
$$\epsilon' = \epsilon + \nu e F d \pm \hbar\omega$$

4.4 Optical phonons

As regards optical phonons in particular, we use the specific factor $c(\mathbf{q})$ introduced in eq.(1.38) and (1.39). In the case of deformation potential, this factor is independent of $\mathbf{q}$ (so we will use $c(\mathbf{q}) = c$), and one more intagration can be performed over the θ variable. The deformation potential scattering probability thus results

$$P_{\nu' n'}(\nu n \mathbf{k}) = \frac{\sqrt{m_x m_y}}{(2\pi)^2 \hbar^3} \left[\begin{array}{c} n \\ n+1 \end{array} \right] c^2 \int \mathrm{d}q_z \left| \langle \nu' n' | e^{\mp i q_z z} | \nu n \rangle \right|^2 . \tag{4.26}$$

For polar interaction, eq.(4.24) must be used. The integrations lef in eq.(4.24) and (4.26) are performed numerically in the simulator.

We present, for example, the transition probabilities for silicon optical phonon and for silicon dioxide polar phonon interactions (Fig.4.2 and 4.3)

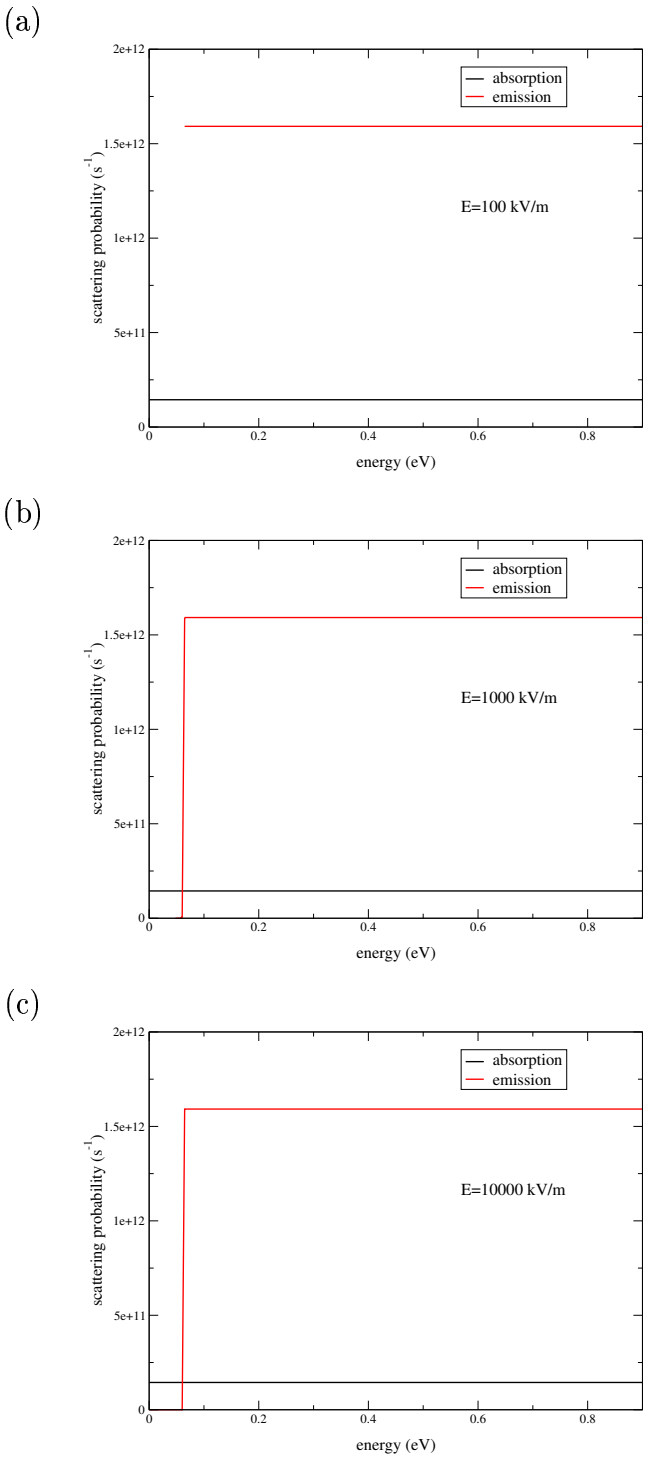

Figure 4.2: *Deformation potential silicon phonon transition probability versus energy for an electron from band 1 to band 1 in any well of the superlattice for three different applied electric fields.*

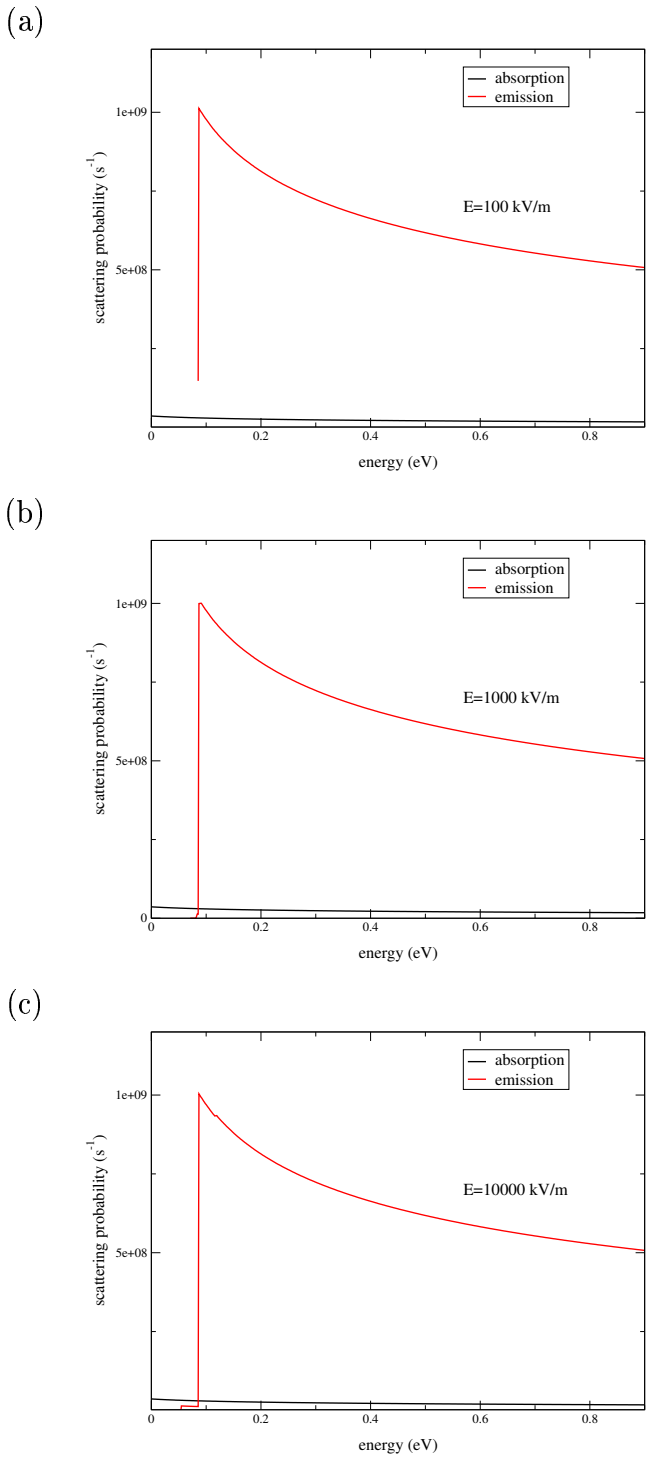

Figure 4.3: *Polar optical phonon transition probability versus energy for an electron from band 1 to band 1 in any well of the superlattice for three different applied electric fields.*

are shown. In particular these probabilities are calculated for the transition from level 1 in well $\nu = 0$ to level 1 in any well ($\nu = 0$ included). In general the transition from well 0 to well 0 is dominant, but when increasing the electric field, little contributions from transition to adjacent wells can be seen in the scattering probability: they give rise to the steps at energies $\hbar\omega \pm \nu eFd$ (with $\nu = 1$) in the emission rates. Moreover, the polar optical transition probability shows the typical decreasing behaviour.

4.5 Monte Carlo simulation of WS transport

Like in the semiclassical case, a Monte Carlo simulation has been performed in order to study transport properties in the framework of the WS functions formalism. Since the electric field has been included in the hamiltonian of the system, and the WS states are eigenstates of this hamiltonian, no acceleration is present between two scattering events. This means that the scattering probability $\Gamma(E)$ is independent of time, since during the time between two scattering the electron does not change its energy. Under this condition, the self-scattering technique, used for the semiclassical simulation of miniband transport, is not necessary and there is no need to maximize the scattering probability. The scattering probability is then used to determine the time between two scattering events: during this time, the electron remains in the same eigenstate $(n, \mathbf{k})$ without any evolution.

The scattering probability has been calculated as $P_{\nu' n'}(\nu n \mathbf{k})$, where the dependence on ν' and n' is explicitely taken into account in order to simply find the final state after the scattering: once chosen the scattering mechanism as described in App.A, the final state $(n, \mathbf{k})$ is automatically identified. The final vave vector $\mathbf{k}'$ is calculated by application of the direct technique to the scattering probability of equations (4.24) and (4.26). Once generated the state after scattering, a new cycle begins.

Since the electric field is applied along the vertical direction, the drift velocity component along the inplane direction is zero and the component along the vertical direction z can be calculated as

$$v_d = \frac{\sum_i \nu_i d}{\sum_i \tau_i} \ , \tag{4.27}$$

where τ_i is the time between two scattering events generated according to eq.(A.4) and d is the superlattice period. Energy and momentum distribution functions along the planes are also collected during the simulation.

4.6 Results

Using the theory and the simulation technique described until now, we have obtained a drift velocity curve (Fig.4.4) similar to that obtained with the miniband transport simulation (Fig.2.7). Nevertheless, the two curves differs in the values of the drift velocity, and in the general position of the curve

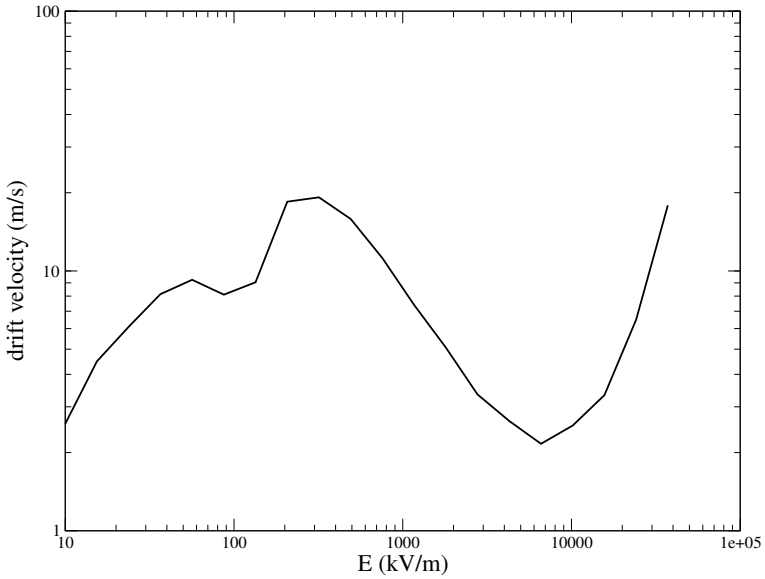

Figure 4.4: *Drift velocity obtained with the WS transport formalism for the studied superlattice.*

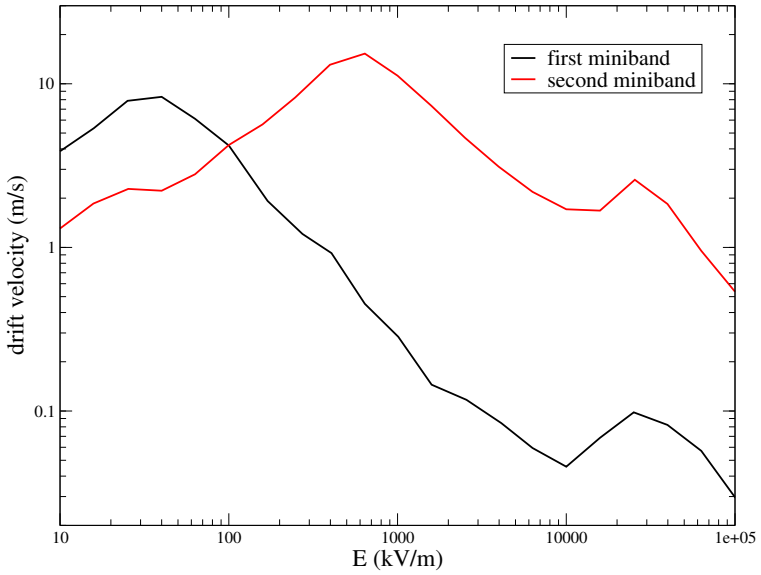

Figure 4.5: *Contributions of the transitions $n = 1 \rightarrow 1$ and $n = 2 \rightarrow 2$ (indicated as first and second miniband in the text) to the overall drift velocity.*

with respect to the electric fields value: the present result is a drift velocity twice as high as the semiclassical one, and all the curve is shifted toward lower fields. The reason of this difference is currently under investigation.

Some new features appear, due to the particular approach of the WS functions. First of all, we can see that two main peaks appear in the low field region of the plot. These two peaks are caused by the contribution to the total drift velocity from WS states derived from Bloch states in the first and the second miniband, as can be deduced from Fig.4.5: different minibands give rise to different contribution to the drift velocity, at different field ranges.

Moreover, using the formalism of the WS functions, new features in the dift velocity curve are present. First of all, when the energy difference between two wells is equal to the phonon energy, a kink in the drift velocity is present, since resonant scattering occurs. These kinks are evindent in the drift velocity curve calculated for each single miniband Fig.4.5 (in this way

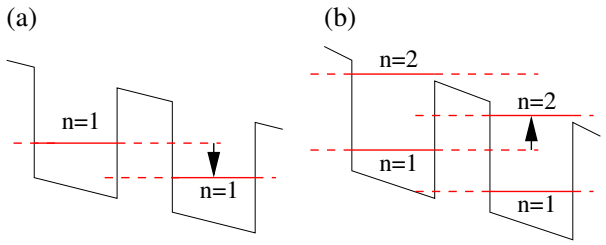

Figure 4.6: *Picture representing the resonance phenomena due to the alignement of the WS levels and the phonon energy. The transitions are represented by the arrow. The same process* $\nu = 0 \rightarrow \nu'$*, depicted for transitions* $0 \rightarrow 1$ *is possible for any* ν'*. The resonance with the optical phonon energy is evident*

interactions with other bands are switched off) in the 10^4 kV/m region. A similar process happens when the energy difference between the first level of a well and the second level of another well is equal or less than a phonon energy: this explains the rapid increase of the drift velocity curve for high electric fields in Fig.4.4. A representation of these two mechanisms is provided in Fig.4.6.

When looking at the energy distribution function (Fig.4.7), a problem is revealed: the sharp step at the initial energy plus the silicon optical phonon energy, indicates that the physical model is probably not sufficiently accurate. A more detailed "step by step" investigation of the electron history has shown that this step is caused by the introduction of scattering mechanisms able to exchange only fixed and high amount of energy . The weak interaction with other wells and levels is not sufficient to distribute electron energy in the right way and this strong peak does not disapper even increasing the statistics in the Monte Carlo simulation.

An indication for this interpretation is that the introducation of a fictitious scattering mechanism with energy of 4 meV, is able to thermalize the energy distribution function as shown in Fig.4.8. This means that for an accurate study of the transport properties, a low energy scattering mechanism,

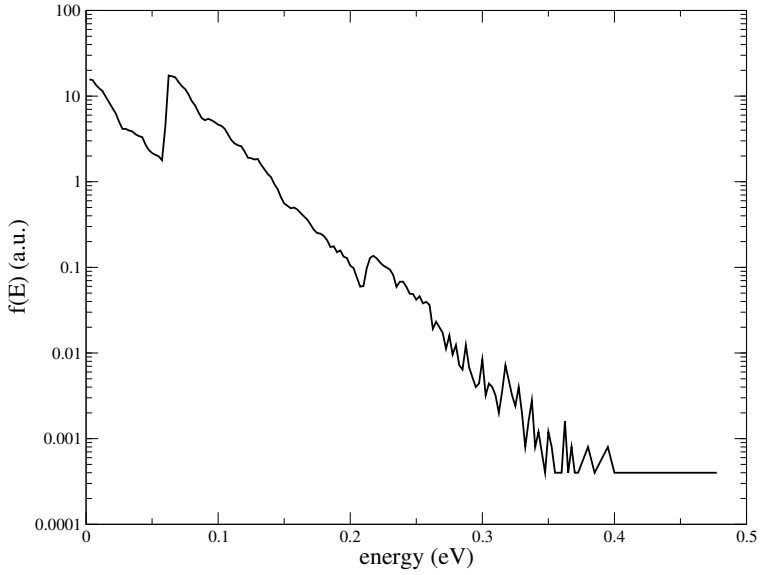

Figure 4.7: *Energy distribution function for electrons in the first subband. A sharp step at the energy of the silicon optical phonon (62 meV) is present.*

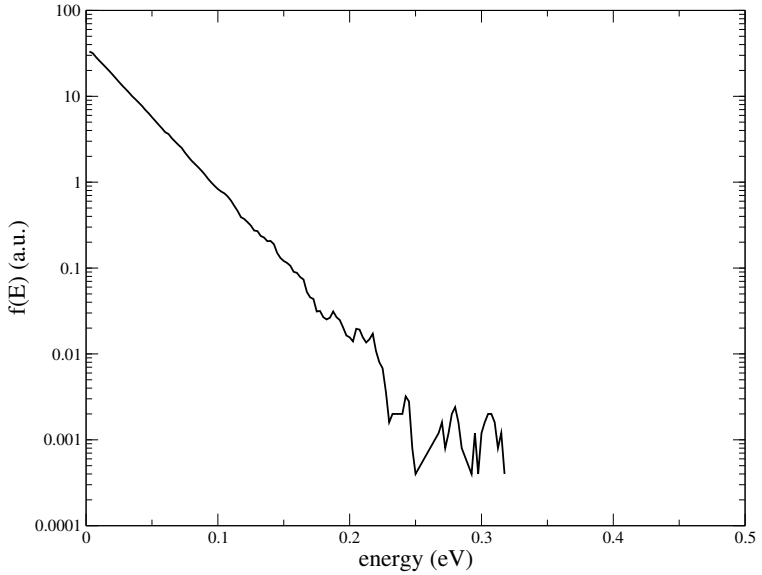

Figure 4.8: *Energy distribution function for electrons in the first subband where a fictitious optical scattering mechanism with 4 meV energy has been introduced.*

such as acoustic phonon scattering, should be useful.

Chapter 5

Proposal for an electroluminescent superlattice-based device

The idea presented in this chapter concerns a proposal for obtaining electroluminescence from a superlattice silicon-based device. The superlattice structure is suitable for its direct gap that should favor recombination, but in general electron density and drift velocity are very low, as seen in the simulation of previous chapter. It is possible to imagine a large oxide barrier after several superlattice periods as in Fig.5.1. In this way, the barrier accumulates electrons, and, when a hole is injected in the opposite direction, a recombination is highly probable.

A simulation has been performed using the Monte Carlo simulation described in Chapter 2.1. An ensemble of electrons, starting at position $z = 0$, has been evolved for a fixed time, collecting, before each scattering, the position on a grid on the z direction. The device is composed of 20 periods of the Si/SiO_2 superlattice used in the previous simulation, and a thick potential barrier. Since this barrier is very thick and high (it is made of a very wide

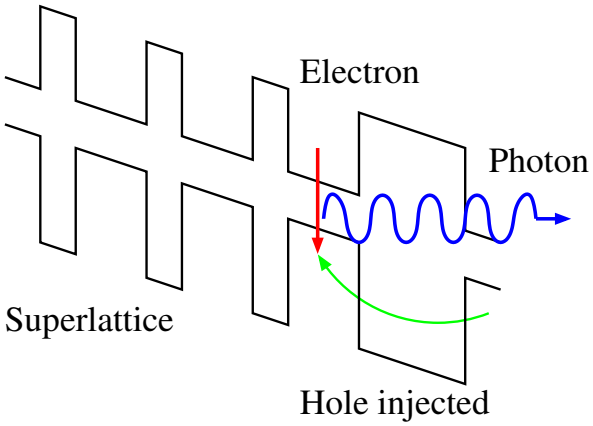

Figure 5.1: *Sketch of the proposed structure and of the recombination mechanism.*

SiO_2 layer), it is possible to model the barrier as an infinite potential. in particular, we have used a model of an elestic barrier.

In Fig.5.2 the electron density has been shown as a function of the z coordinate. It can be seen that near the barrier, the electron density increases of about one order of magnitude. Since the recombination rate roughly depends on the product of electron and hole density [48], it can be deduced that radiative recombination is highly favoured.

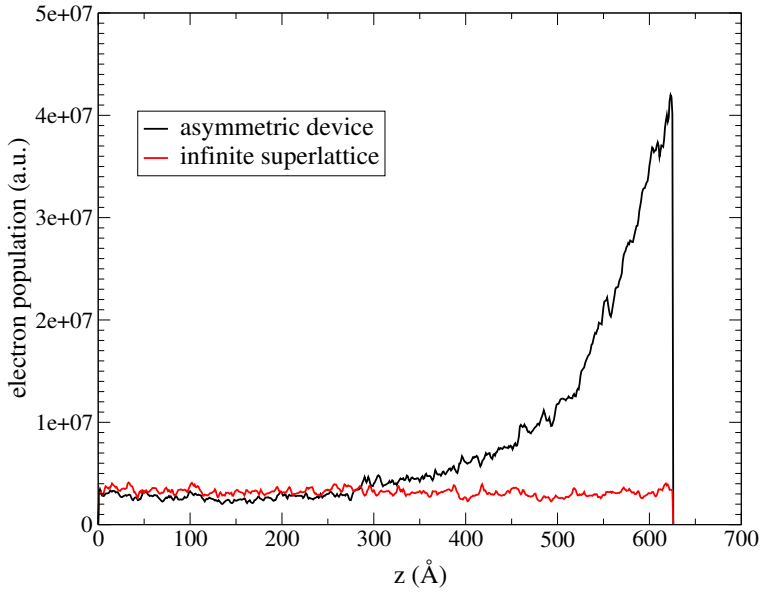

Figure 5.2: *Spatial distribution (black line - arbitrary units) of the electron along the superlattice structure. The distribution in an infinite superlattice (red line) is reported for comparison.*

Part II

Transport in quantum wires

Chapter 6

Coherent transport in quantum wires assisted by Surface Acoustic Waves

6.1 Introduction

Since the discovery that quantum data propcesing can be implemented, almost a decade ago, efforts have been devoted for identifying physical systems able to relize a qubit and the basic transformations needed for quantum computation. The number of systems proposed is still limited and it is difficult to find a system that allows one to set up and connect an arbitrary number of qubits. Recently, the group where this work has been developed has proposed a solid state implementation of quantum logic gate devices [49]. The system proposed is based on coherent propagation of electrons in coupled semiconductors quantum wires, where the state of the qubit is represented by the state of the electron and can be controlled by proper design of the system.

This system not only stisfies the properties needed for the realization of

quantum gates, but it is also able to satisfy the "Di Vincenzo" [50] check list for a thinkable quantum computer since (a) it is compact, reliable and reproducible; (b) the output of a quantum gate can be used as input for the next gate; (c) it is integrable with conventional electronics.

The classical information theory is based on the binary encoding of the information: any integer N is represented by an ordered sequence of n bits a_i, according to

$$N = \sum_{i=0}^{n-1} a_i 2^i \tag{6.1}$$

where $a_i \in 0, 1$. Any bit can assume only one of the two possible values: 0 or 1. If a bit of information is encoded using a state of a system described by quantum mechanics, the bit can be in any superposition of 0 and 1. In fact, the states 0 and 1 are associated with two specific eigenstates ($|\psi_0\rangle$ and $|\psi_1\rangle$ respectively) of a suitable observable, and now the system can be in any state

$$|\psi\rangle = c_0|\psi_0\rangle + c_1|\psi_1\rangle \tag{6.2}$$

with c_0 and c_1 are complex numbers that satisfy $|c_0|^2 + |c_1|^2 = 1$. This means that the quantum analog of a bit, the qubit [51], can be simultaneously in both states: if we measure the qubit we can obtain the value 0 and 1 with probability $|c_0|^2$ and $|c_1|^2$ respectively. The two basis states of the qubit are indicated as $|0\rangle$ and $|1\rangle$.

When information is encoded in an array of qubits and processed with a "quantum machine" able to preserve superposition of quantum states, it is possible to create an input state that is a linear superposition of m classical inputs, then the output of the elaboration will be the same superposition of the corresponding m classical results. In this case the quantum computing presents a kind of "natural" parallelism.

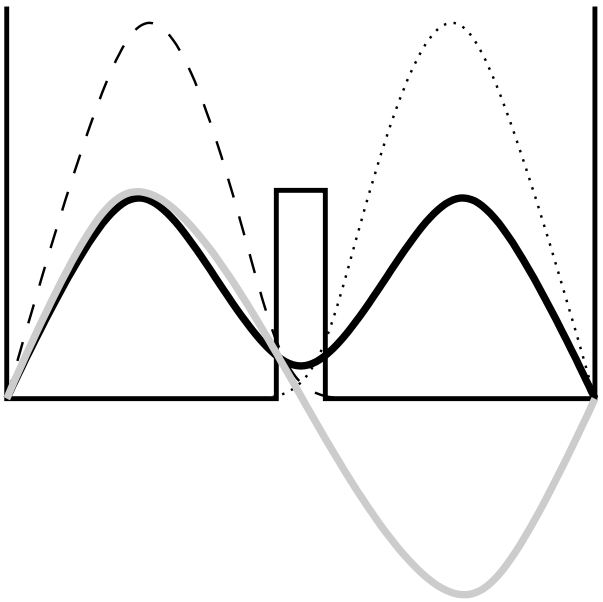

Figure 6.1: *Transverse potential of the two quantum wires. The symmetric and antisymmetric wave function are drawn together with their sum and difference that are the states* $|0\rangle$ *and* $|1\rangle$ *respectively. (From [49])*

6.2 Physical system and principles

The basic device considered here consists of two parallel intrinsic $GaAs/Al_xGa_{1-x}As$ quantum wires, operating at very low temperature in order to have a negligible electron density in conduction band and to minimize electrons-phonon interactions, responsible of the decoherence process. The transverse potential of the system can be seen as a double square-well potential (Fig.6.1). We suppose that the potential barrier separating the two wires is sufficiently high to make their tunneling probability negligible. In the middle of the device, a coupling window is opened in the barrier, thus allowing electron transfer between the two wires (Fig.6.2).

Let us consider an electron injected into one of the two wires, in a region of the device, where the potential barrier is high. The defined potential is separable along the longitudinal and transverse direction of the system.

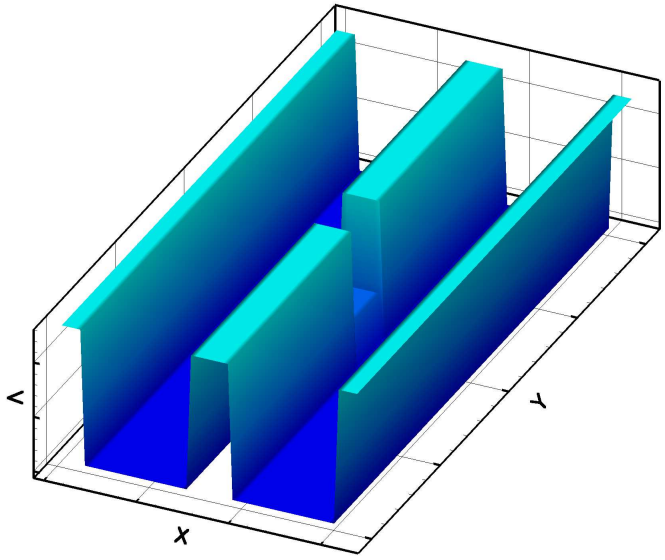

Figure 6.2: *Overall potential of the two-wires structure.*

Here we suppose that the transverse barrier is able to keep the electron in the transversal ground state of one wire, while, in the longitudinal direction, the state of the electron is assumed to be a minimum uncertainty wave packet with a wave-vector centered around k_0. The initial state of the system can then be written as

$$\psi(x,y) = \sqrt{\frac{2}{L}}\cos\left[\pi\frac{x-x_0}{L}\right]\frac{1}{\sqrt{\sigma\sqrt{2\pi}}}e^{-\left(\frac{y-y_0}{2\sigma}\right)^2}e^{-ik_0y}\ , \tag{6.3}$$

where x_0 is chosen to be the center of the left well (x_1 will denote the center of the right well).

Let us define the state of the qubit as $|0\rangle$ if the electron is injected in the left wire, and $|1\rangle$ if it is in the right wire. Let us now introduce the coupling window between the two wires. In this region the two wires are strongly interacting. The transversal wave function, localized in one of the two wires, can be written with a good approximation as superpositions of the even ψ_e and the odd ψ_o eigenstates of the coupled system:

$$|0\rangle \;=\; \frac{1}{\sqrt{2}}(|\psi_e\rangle + |\psi_o\rangle) \tag{6.4}$$

$$|1\rangle \;=\; \frac{1}{\sqrt{2}}(|\psi_e\rangle - |\psi_o\rangle) \;. \tag{6.5}$$

The evolution of these two states is given by the evolution of the two eigenstates ψ_e and ψ_o

$$\begin{aligned}
|0\rangle &\rightarrow \frac{1}{\sqrt{2}}(|\psi_e\rangle e^{-i\omega_e t} + |\psi_o\rangle e^{-i\omega_o t}) \\
&= e^{-i\omega t} e^{i\frac{\theta}{2}} \left(\cos\frac{\theta}{2}\,|0\rangle + i \sin\frac{\theta}{2}\,|1\rangle \right) \\
|1\rangle &\rightarrow \frac{1}{\sqrt{2}}(|\psi_e\rangle e^{-i\omega_e t} - |\psi_o\rangle e^{-i\omega_o t}) \\
&= e^{-i\omega t} e^{i\frac{\theta}{2}} \left(i \sin\frac{\theta}{2}\,|0\rangle + \cos\frac{\theta}{2}\,|1\rangle \right) \;,
\end{aligned} \tag{6.6}$$

where $\theta = (\omega_o - \omega_e)t$. This means that, in the coupling region, the electron wave function oscillates between the two wires with a frequency $\omega_o - \omega_e$ (this kind of oscillation has been experimentally observed [52]). Then, by an accurate tuning of the physical parameters (the window length, the wires and the potential barrier widths) the number of oscillations can be controlled, thus allowing to determine the fraction of electron wave function transmitted in each of the two channels.

6.3 Basic logic gates with quantum wires

In order to perform any quantum bit transformation, as in the classical information theory, a minimum set of quantum gates is necessary: these are called "universal set of gates".

Among all possible quantum gates, we are interested in two particular single-qubit operations: the "quantum NOT" and the "beam splitter". Both of them are based on the basic device whose geometry has been described in the previous section: they only differ for the length of the coupling window. The quantum not gate is able to perform the shift of the electron injected in

one wire to the other wire

$$|0\rangle \rightarrow |1\rangle \ , \quad |1\rangle \rightarrow |0\rangle \tag{6.7}$$

while the beam splitter is able to separate the wave function into two parts running in the two wires, for example

$$|0\rangle \rightarrow \alpha|0\rangle + \beta|1\rangle \ . \tag{6.8}$$

The functionality of the proposed system to perform the above operations has been verified through numerical simulations. Simulations are performed using a finite difference method for solving the two-dimensional time-dependent Schrödinger equation of the system. The parameters of the simulation are reported in App.C.1.

The simulation of the quantum NOT gate shows (Fig.6.3) that when the electron, once injected in the left wire, reaches the coupling window, the oscillation starts between the two wires and, since the length of the window is calibrated to obtain half an oscillation, the final state of the electron is comletely localized in the right wire. When the coupling window length is reduced in order to let the wave function oscillate for a quarter of a period, the quantum beam splitter is obtained (Fig.6.4).

6.4 Introduction of the SAW potential

In order to avoid computational errors in a wide network of this kind of quantum devices, a redundance of information can be obtained by injecting a large number of electrons in sequence [53], with the condition that one electron cannot interact with the previous or the following one. Moreover, as can be seen in Fig.6.3 and Fig.6.4, the wave packet is subject to quantum mechanical broadening during its propagation. This broadening may generate problems to succesive quantum eleborations. A possible solution to both

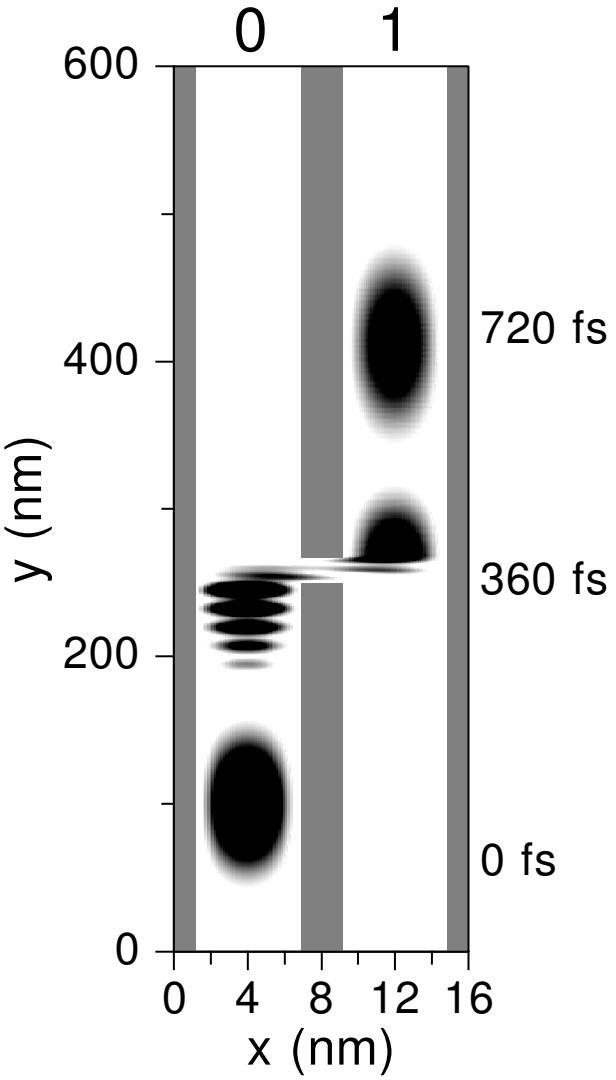

Figure 6.3: *Square module of the electron wave function evolving in the quantum NOT device a three different times. The length of the window is 16 nm and it is calibrated to obtain half an oscillation (see eq.6.6). (From [49])*

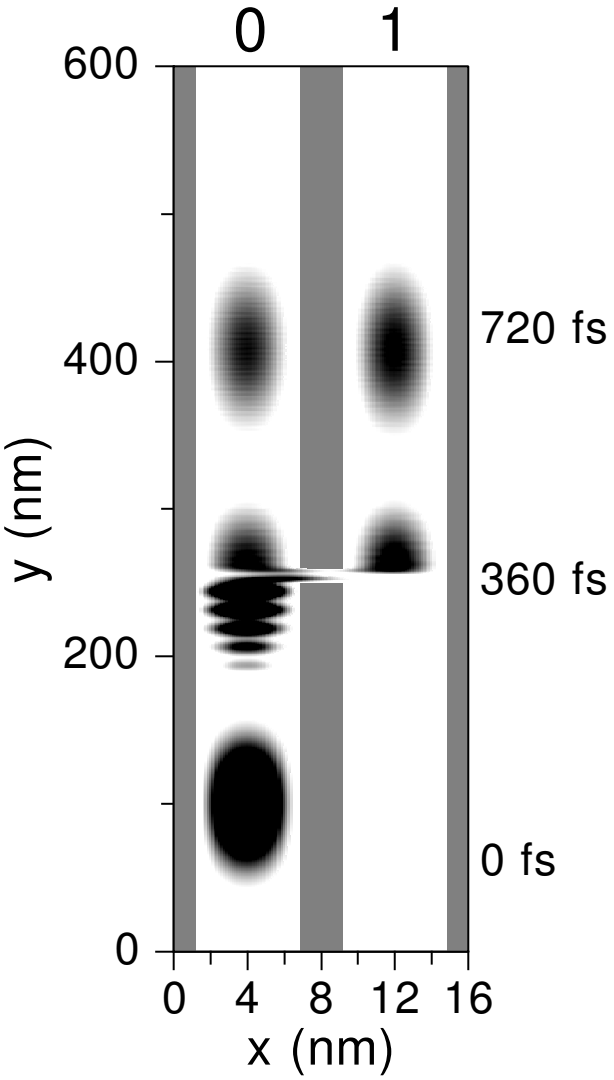

Figure 6.4: *Square module of the electron wave function evolving in the beam splitter device a three different times. The length of the window is now set to 8 nm to obtain a quarter of an oscillation. (From [49])*

problems is to use surface acoustic waves (SAW) for injecting and driving electrons in the device.

Surface acoustic waves have been used in the last years as a tool to realize, in a very controlled way, single electron transport and counting in solid state nano-devices [54, 55, 56]. In the following we have proved that SAW can be used for this task, performing the simulation of the coherent evolution of electrons in two coupled quantum wires assisted by the SAW. For the proposed devices, such a method presents two main advantages with respect to the free propagation of a single electron along the quantum wire (where injection is provided, for example, by a single electron pump [57]): (1) two or more electrons can be injected simultaneously in different wires: in fact in the lead region electrons are collected in the minima of the SAW forming a line perpendicular to the wires, and reach simultaneously the entrance to the wires; (2) since the electron wave function is embedded in a "moving quantum dot" formed by the minimum of the SAW and the wire barriers, its spread does not increase during the propagation. This condition should allow the creation of longer quantum gate networks with respect to the case of purely ballistic propagation[53].

To study the effect of the SAW-driven propagation on the functionality of the quantum-gates, we have used the same 2D time-dependent Schrödinger solver used for the results reported in the previous sections, where the ability to account for a potential explicitly dependent on time has been added. A number of simulations have been performed, where the moving sinusoidal potential of the SAW is added to the potential profile representing the two coupled quantum wires.

The initial wave function, fully localized in a wire, has been chosen as:

$$\Psi(x, y, t = 0) = \phi(x)\chi(y)e^{i\frac{m^* v_s}{\hbar}y} \tag{6.9}$$

where $\phi(x)$ is the ground eigenstate of the wire potential in the x direction

(calculated as in eq.(6.3)), $\chi(y)$ is the ground eigenstate of a minimum of the potential representing the SAW (at a fixed time) in the y direction, m^* is the GaAs effective mass of the electron and v_s is the sound velocity in the material equal to the initial velocity of the carrier. The exponential factor is introduced in the initial condition in order to provide to the electron a drift velocity equal to that of the sound wave.

6.5 Results

In this section, the results of the simulations are presented. In particular, the same operations (quantum NOT and beam splitter) described above are simulated with the introduction of the SAW potential. The SAW is much slower than the wave packet of previous simulations and the device crossing time for the electron will be much higher. For this reason, the geometry of the device has been modified: in particular wider barrier and wires and shorter coupling window have been used. The SAW parameters are calibrated on the transverse acoustic phonon mode of GaAs. For all simulation parameters, see App.C.2.

Fig.6.5 shows the evolution of the square module of the wave function at three different time steps: (a) before reaching the coupling window, (b) passing through the coupling window, and (c) after the window, for the quantum NOT gate. From the calculation it turns out that 99.2% of the initial wave function is transferred in the second wire. The beam splitter operation is presented in Fig.6.6. In this case the fraction of transferred wave function results to be 51.3%.

Results show that the SAW potential is very useful in order to prevent the spreading of the electron wave function, that is evident without the SAW potential (Fig.6.3 and Fig.6.4), and reducing undesired reflection effects due to the interaction with the coupling window. The former property uis very

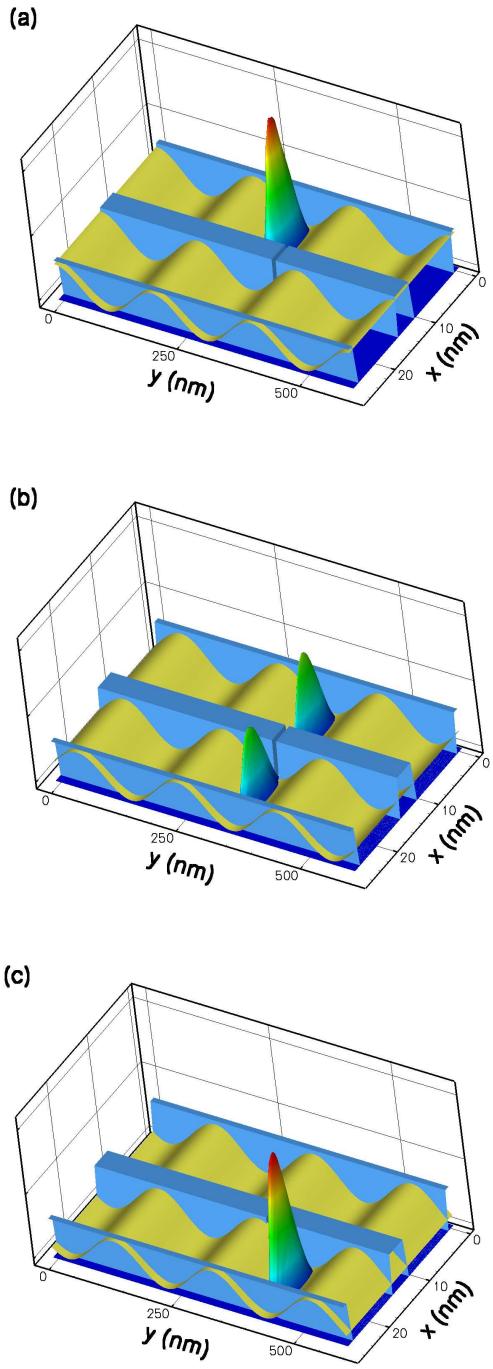

Figure 6.5: *Evolution of the square module of the wave function at three different time steps: (a) before reaching the coupling window ($t = 0$), (b) passing through the coupling window ($t = 19.8\ ps$), and (c) after the window ($t = 40ps$), for the quantum NOT gate. The coupling window is 7 nm long. Note that in the picture are also represented, on arbitrary scales, the shape of the two-wires potential and of the SAW potential.*

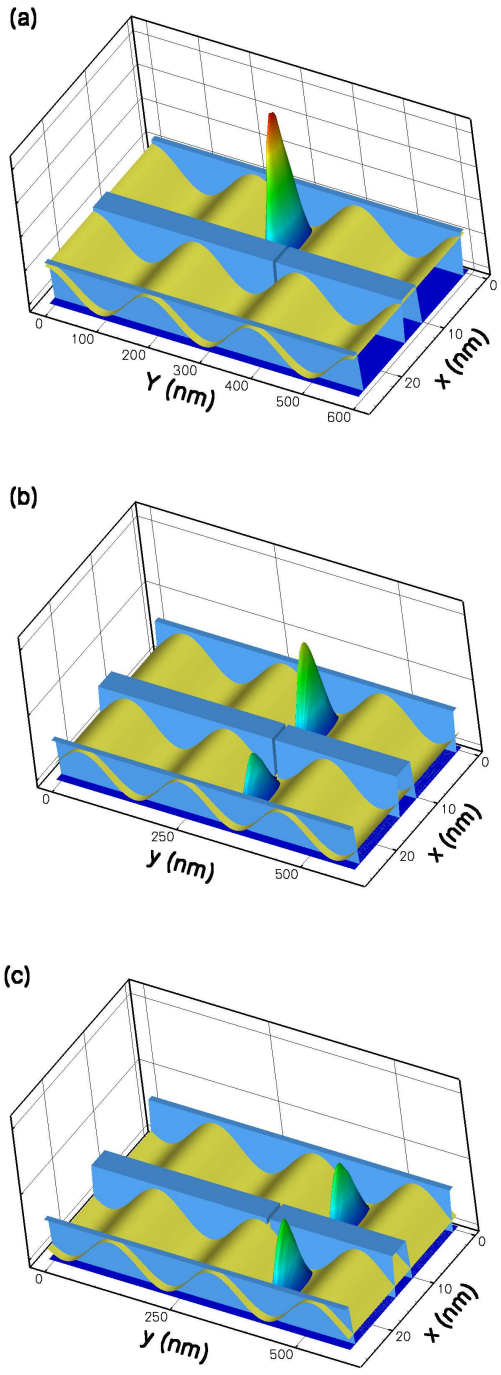

Figure 6.6: *Same as in Fig.6.5, for the case of a beam splitter. The length of the coupling window is now 5 nm.*

useful for a possible realization of a quantum bit network, since the electron wave function remains narrow and well localized in the device. Moreover, the SAW confining potential is very efficient for the confining of the electron as can be seen from the plot of the Fourier transform of the wave packet along the longitudinal direction (Fig.6.7). The electron initial velocity of eq.(6.9) has been setup different from the SAW velocity and it can be seen that the fourier transformed wave packet oscillates around the value representing the velocity of the SAW. In real space this phenomenon is associated with a real oscillation of the wave packet around the minimum of the SAW potential, without escaping. The oscillation observed in the width of the transformed wave packet is caused by the interaction of the packet with the potential barrier of the SAW. If no SAW potential were present, the fourier components would not change in time but the wave packet would be subject to quantum mechanical spreading.

6.6 Future developments

The introduction of the SAW in modeling the dynamics of electrons in systems of coupled quantum wires has proven to be very promising. The next steps will be applying such method to the study of more complex logic networks (see for example the two-qubits gates described in Ref.[49]), and to systems modelled with a more realistic potential profile of the quantum wires obtained by means of a Schrödinger-Poisson solver. Moreover, we are now trying to simulate the same device, with lower SAW potential, in order to reproduce experimental conditions.

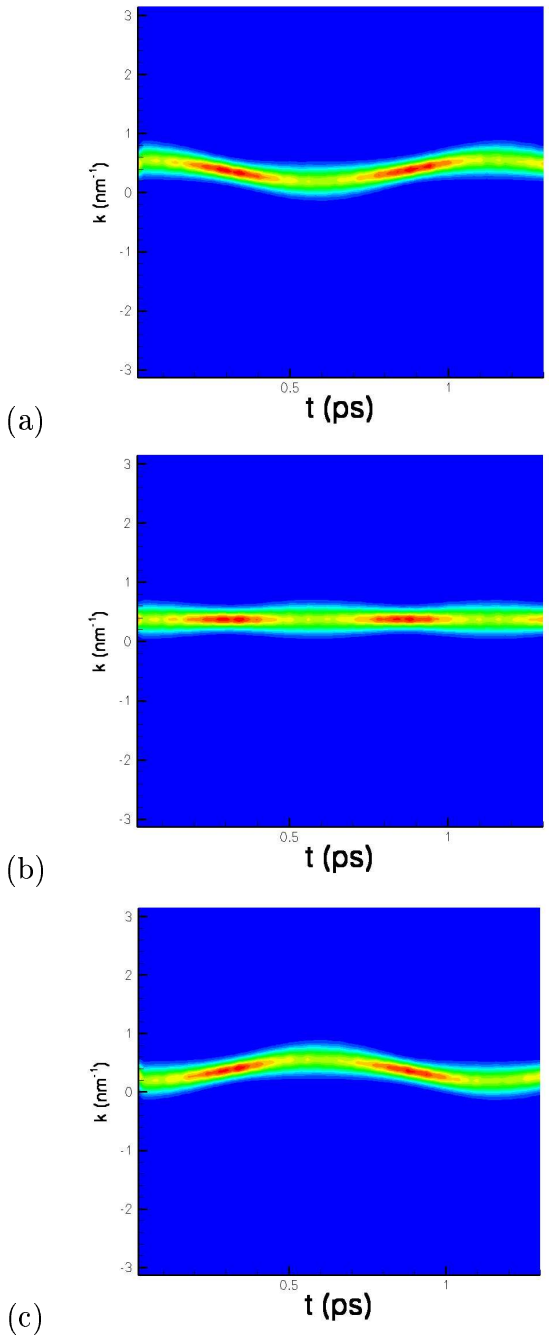

Figure 6.7: *Fourier transformed packet along the longitudinal direction for a packet velocity (a)half (b)equal and (c)double with respect to the SAW velocity. The oscillation are caused by the SAW confining potential.*

Part III

Appendixes

Appendix A

Monte Carlo method for transport

In this appendix we describe the fundamentals of the semiclassical Monte Carlo method for transport simulations. As regards the Monte Carlo simulation used with the Wannier-Stark functions, detailes are reported in the corresponding chapter.

A.1 The Boltzmann equation

In order to study carrier transport, the motion of the carriers has to be taken into examination, when electric or magnetic fields are applied. In the following we describe the theory based on the semiclassical approximation. According to this approximation, carrier wave packets are supposed to be localized in space to have neglectable dimension with respect to the external potential variation ranges and mean free paths; at the same time the Fourier transformed packet is supposed to be small compared to the Brillouin zone. In this way the electron can be identified with the coordinates $(\mathbf{r}, \mathbf{k}_0)$ of the centres of the wave packets in real and reciprocal space respectively, as a

classical particle. The semiclassical dynamics states that the centre of the wave packet follows a semiclassical trajectory

$$\hbar\frac{\mathrm{d}\mathbf{k}_0}{\mathrm{d}t} = e\left(\mathbf{E} + \frac{1}{c}\mathbf{v}_g \wedge \mathbf{B}\right) \ , \tag{A.1}$$

where $\mathbf{v}_g$ is the carrier group velocity. This equation means that a carrier subject to external fields behaves like a classical particle with momentum $\hbar\mathbf{k}_0$ subject to the same field. The difference between this equation and the classical equivalent, is that $\mathbf{k}_0$ is the pseudomomentum of the electron and the particle energy is described by the band.

In this semiclassical picture, the fundamental role is played by the distribution function $f(\mathbf{r}, \mathbf{k}, t)$, proportional to the carrier density in phase space. When this function is normalized to 1, it represents the density of probability to find an electron in a state $(\mathbf{r}, \mathbf{k})$. The evolution of the distribution function is governed by the Boltzmann equation

$$\frac{\partial f}{\partial t} + \mathbf{v}(\mathbf{k}) \cdot \nabla_{\mathbf{r}} f + \frac{\mathbf{F}}{\hbar} \cdot \nabla_{\mathbf{k}} f = \left(\frac{\partial f}{\partial t}\right)_{coll} \ , \tag{A.2}$$

where $\mathbf{F}$ is the total force acting on the electron, and the right term (*collision term*) is the variation of the distribution function caused by the scattering mechanisms. Once known the distribution function, every physical quantities of interest can be deduced from it.

In a homogeneous situation the collision term can be expressed as the difference between the number of carriers entering and exiting a volume $\mathrm{d}\mathbf{k}$ owing to scattering mechanisms, per unit time

$$\left(\frac{\partial f}{\partial t}\right)_{coll} = \frac{V}{(2\pi)^3}\int \mathrm{d}\mathbf{k}' \left[f(\mathbf{k}')P(\mathbf{k}', \mathbf{k})(1 - f(\mathbf{k})) - f(\mathbf{k})P(\mathbf{k}, \mathbf{k}')(1 - f(\mathbf{k}'))\right] \tag{A.3}$$

where $P(\mathbf{k}, \mathbf{k}')$ is the transition probability and the distribution functions are present with their complementary term to unit, in order to account for the Pauli exlusion principle. In general the transition probability P is included using the fermi golden rule, i.e. the first-order time-dependent perturbation theory, where the interaction hamiltonian is the perturbation.

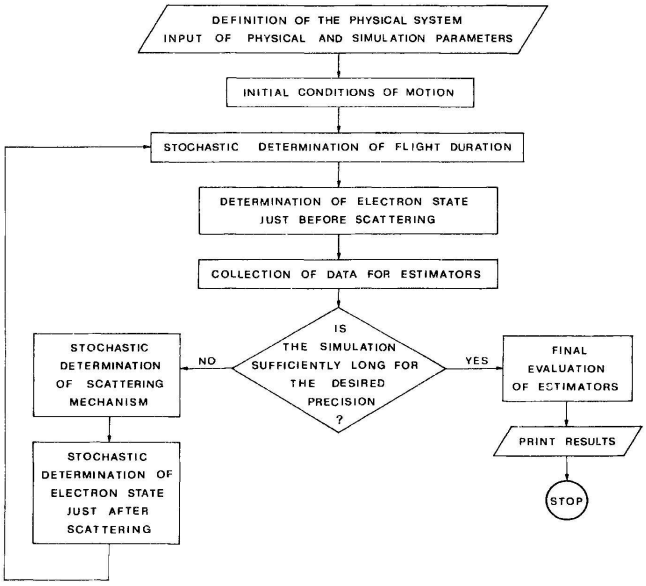

Figure A.1: *General scheme of a single-particle Monte Carlo algorithm for transport.*

A.2 The general technique

The Monte Carlo method is based on the generation of random numbers according to well defined probabilities, and can be applied to a great variety of problems. In the case of carrier transport, the evolution of a particle, interacting with various potentials, can be fully simulated in the phase space. If we want to simulate a stationary simulation, it is sufficient the time-evolution of only one particle: in practice we are using the ergodicity hypothesys, supposing that the time average of a single particle is equal to the enseble average. point.

The general sequence of a Monte Carlo algorithm consists of different steps (Fig.A.1). After the definition of the physical system (material, scattering mechanisms, external fields, simulation parameters) and of the initial state of the motion, the motion starts. First of all, the scattering probabilities are used to define a mean scattering time τ_0. If the scattering probability

is independent of $\mathbf{k}$, then $\tau_0 = \frac{1}{P_0}$, otherwise we can define a maximized probability $P_0 = \max P(\mathbf{k})$, having introduced, in such a way, a fictitious mechanism, called *self-scattering*, whose final state is equal to the initial one. Now, $P[\mathbf{k}(t)]\mathrm{d}t = \frac{1}{\tau_0} e^{\frac{\tau}{\tau_0}}$ is the probability for an electron to suffer a scattering at the interval $\mathrm{d}t$ around time t. The simulation may then proceed by generating the *free flight time* as follows [44]

$$t_r = -\tau_0 \ln(r) \tag{A.4}$$

with r a random number between 0 and 1. During this time physical laws, such as acceleration produced by the electric field, are applied to the electron, and all the physical quantities, we are interested in, are collected at the end of this *flight*. Generally, the physical quantities of interest are mean energy, derift velocity, energy and momentum distributions, covered space.

Then, a scattering occurs. In order to determine which scattering is chosen, the different probabilities $P_i(\mathbf{k})$ of the i-th process (including the self scattering process) are calculated, then a random number r' is chosen between 0 and $\Gamma(\mathbf{k}) = \sum_i P_i(\mathbf{k})$. The n-th scattering mechanism is chosen if

$$\sum_{i=1}^{n-1} P_i < r < \sum_{i=1}^{n} P_i \ , \tag{A.5}$$

the probability of this choice is proportional to P_i.

The final state of the particle after the transition is randomly determinded according to the differential cross section of the particular scattering mechanism occured. At this moment a new cycle begins and the procedure goes on until the desired precision for the result is reached.

Appendix B

Other calculations

B.1 Effective hamiltonian for Si(111)/SiO_2

B.1.1 The general case

In this section, the effective hamiltonian is found for a Si/SiO_2 superlattice, with silicon crystal oriented in any direction with respect to the superlattice planes. Let us indicate the coordinate of a vector with respect to the silicon crystal directions as $r = (x, y, z) = (x_1, x_2, x_3)$, and the same vector with respect to the superlattice (SL) system a $R = (X, Y, Z) = (X_1, X_2, X_3)$. The hamiltonian will be the following

$$\begin{aligned} \widehat{H} &= -\frac{\hbar^2}{2m_{xx}}k_x^2 - \frac{\hbar^2}{2m_{yy}}k_y^2 - \frac{\hbar^2}{2m_{zz}}k_z^2 + V(Z) \\ &= \frac{\hbar^2}{2}k_{x_i}\left(\frac{1}{m}\right)_{ij}k_{x_j} + V(Z) \end{aligned} \tag{B.1}$$

since the mass tensor is diagonal in the Si-crystal system, and the Einstein notation for repeated indexes is used. A unique coordinate system (namely the SL system) is now to be used in the hamiltonian. The rotation between the two systems, described by an orthogonal matrix A, is such that

$$X_i = A_{ij}x_j \tag{B.2}$$

$$x_i = A^{-1}_{ij} X_j = A^T_{ij} X_j = A_{ji} X_j \quad . \tag{B.3}$$

It is easy to demonstrate that the momenta follow the same transformation rule, as can be seen from the transformation of the partial derivative;

$$\frac{\partial}{\partial X_i} = \frac{\partial}{\partial x_j}\frac{\partial x_j}{\partial X_i} = A^T_{ji}\frac{\partial}{\partial x_j} = A_{ij}\frac{\partial}{\partial x_j} \tag{B.4}$$

from which we define now $K_i = A_{ij} k_j$. The transformed Hamiltonian in the SL system becomes now

$$\begin{aligned} \widehat{H} &= \frac{\hbar^2}{2} A^T_{il} K_l \left(\frac{1}{m}\right)_{ij} A^T_{jm} K_m + V(Z) \\ &= \frac{\hbar^2}{2} K_l \left(\frac{1}{M}\right)_{lm} K_m + V(Z) \end{aligned} \tag{B.5}$$

where

$$\left(\frac{1}{M}\right)_{lm} = A_{li}\left(\frac{1}{m}\right)_{ij} A^T_{jm} \tag{B.6}$$

is the effective mass tensor expressed in the SL coordinate system. Since the Si-lattice effective mass tensor is diagonal, it is possible to write $\left(\frac{1}{m}\right)_{ij} = \left(\frac{1}{m}\right)_{ij}\delta_{ij}$, then $\left(\frac{1}{M}\right)_{lm} = A_{li}\left(\frac{1}{m}\right)_{ii} A^T_{im}$, where the summation over j has been eliminated by the Kronecker delta.

B.1.2 The Si(111) calculation

Let us consider now a superlattice with the planes orthogonal to the (111) direction. We have chosen the orientation of the two coordinate systems as shown in the figure (Fig.B.1), with Y lying on the xy plane along the 45° direction. It can be easily shown that in this geometry the transformation matrix is

$$A = \frac{1}{\sqrt{6}}\begin{pmatrix} -1 & -1 & 2 \\ \sqrt{3} & -\sqrt{3} & 0 \\ \sqrt{2} & \sqrt{2} & \sqrt{2} \end{pmatrix} \quad . \tag{B.7}$$

In the case of silicon, the six ellipsoidal minima of the band structure are equivalent with respect to the Z direction, since the system is invarant

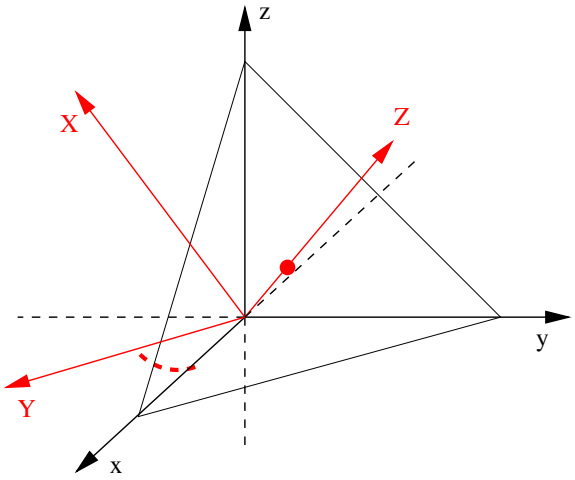

Figure B.1: *Relative position of the Si* (xyz) *and SL* (XYZ) *coordinate systems*

under any permutation of the x, y, z axes. So we can develope the theory with restriction to a particular band minimum, i.e. the (001) minimum; in this way it is possible to use $m_{11} = m_{22} = m_t$ and $m_{33} = m_l$, the transverse and longitudinal silicon effective masses. In this way we find the effective mass tensor in the SL system

$$\frac{1}{M} = \begin{pmatrix} a & 0 & d \\ 0 & b & 0 \\ d & 0 & c \end{pmatrix} \tag{B.8}$$

where $a = \frac{1}{3}\left(\frac{1}{m_t} + \frac{2}{m_l}\right)$, $b = \frac{1}{m_t}$, $c = \frac{1}{3}\left(\frac{2}{m_t} + \frac{1}{m_l}\right)$, $d = \frac{1}{3}\left(-\frac{\sqrt{2}}{m_t} + \frac{\sqrt{2}}{m_l}\right) = \sqrt{2}(a - c)$.

Using this substitution, the effective mass hamiltonian in the SL system is finally

$$\widehat{H} = \frac{\hbar^2}{2}\left[aK_X^2 + bK_Y^2 + cK_Z x^2 + 2\sqrt{2}(a - c)K_X K_Z\right] + V(Z)\ . \tag{B.9}$$

B.2 Mean kinetic energy in SL minibands

The SL under investigation is a quasi-2D system: the electron dispersion is assumed to be parabolic in the xy-plane and a nearly flat cosine shape in the z direction. So we can expect a mean value, for the kinetic energy K, between the 2-dimensional k_BT and the 3-dimensional $\frac{3}{2}k_BT$. In this section we perform this calculation. The starting point is the standard statistical expression [58]

$$\bar{K} = -\frac{\partial}{\partial\beta}\ln\int_{-\infty}^{+\infty} e^{-\beta\epsilon(\mathbf{p})}\mathrm{d}\mathbf{p} \ . \tag{B.10}$$

The electron kinetic energy is measured starting from the minimum of the miniband. eq. (1.30) can be rewritten as $\epsilon(\mathbf{p}) = \epsilon_x + \epsilon_y + \Delta(1 - cos\frac{p_z}{\hbar}d)$ (where $\Delta = \tilde{t}$ in eq.1.30), and the above definition becomes:

$$\bar{K} = -\sum_{i=1}^{3}\frac{\partial}{\partial\beta}\ln\int_{-\infty}^{+\infty} e^{-\beta\epsilon_i(p_i)}\mathrm{d}p_i = \sum_{i=1}^{3} K_i = \frac{1}{\beta} + K_3 \ . \tag{B.11}$$

The mean kinetic energy is $K_1 = K_2 = \frac{1}{2\beta}$ for the parabolic degrees of freedom, while for the z direction it is

$$\bar{K}_z = \Delta - \frac{\partial}{\partial\beta}\ln I(\beta,\Delta) \ , \tag{B.12}$$

where

$$I(\beta,\Delta) = 2\frac{\hbar}{d}\int_0^{\pi} e^{\beta\Delta\cos\xi}\mathrm{d}\xi \ . \tag{B.13}$$

If we perform the substitution $c = -\cos(\xi)$

$$\begin{aligned} I(\beta,\Delta) &= 2\frac{\hbar}{d}\int_{-1}^{1}(1-c^2)^{-\frac{1}{2}}e^{\beta\Delta c}\mathrm{d}c \\ &= 2\frac{\hbar}{d}\sqrt{\pi}\Gamma\left(\frac{1}{2}\right)\mathcal{I}_0(\beta\Delta) \ , \end{aligned} \tag{B.14}$$

here Γ is the factorial function, and $\mathcal{I}_0(\beta\Delta)$ is the Bessel function. Substituting the last result in eq.(B.12), and remembering $\frac{1}{2\beta} = k_BT$, we have the final form

$$\bar{K}_z(T,\Delta) = \Delta - \left[\frac{\partial}{\partial\beta}\ln\mathcal{I}_0(\beta\Delta)\right]_{\beta=\frac{1}{k_BT}} \ . \tag{B.15}$$

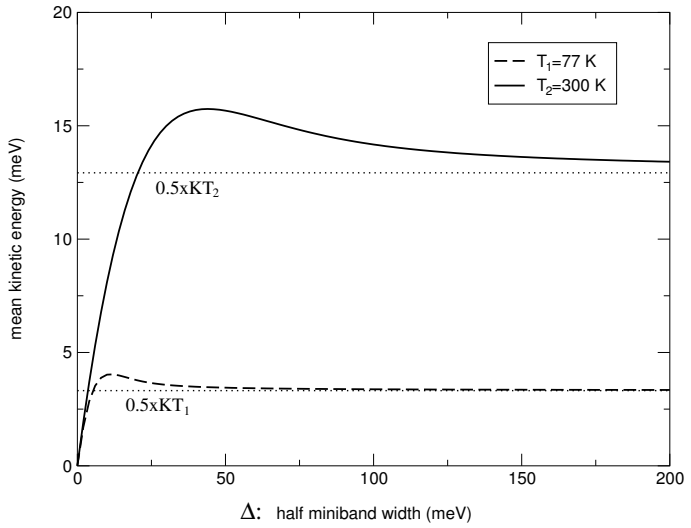

Figure B.2: *Mean kinetic energy in a SL miniband vs* Δ *(half of the miniband width).*

The result can be plotted numerically (Fig.B.2): the graph shows that for low Δ the 1D kinetic energy is between 0 and k_BT. This value increase with Δ and becomes greater than k_BT: this is due to the particular form of the miniband. At larger Δ the value tends to the parabolic limit $k_BT/2$.

Appendix C

Parameters used in the calculations

C.1 Superlattice parameters

In Table C.1 the values used for the simulation of transport in superlattice and the source they are taken from.

C.2 Quantum wires parameters

In Table C.2 the physical parameters used for the simulation of transport in coupled quantum wires. In particular, for the sound velocity, we have used data relative to transverse acoustic phonons in GaAs.

Physical quantity	**Value [Ref.]**
longitudinal effective mass in Si	$m^* = 0.97$ [59]
transverse effective mass in Si	$m^* = 0.19$ [59]
effective mass in SiO_2	$m^* = 0.3$ [36],[37]
conduction band offset	CBO=3.1 eV [60]
lattice temperature	T=300 K
Si optical phonon energy	E=60 meV [44]
Si optical coupling constant	$D_t K = 8 \cdot 10^8$ eV/cm [44]
oxide nonpolar phonon energy	E=132 meV [61]
oxide optical coupling constant	$D_t K = 2 \cdot 10^9$ eV/cm [61]
oxide first polar phonon energy	E=63 meV [61]
first polar optical constant	$\frac{1}{\epsilon_+} - \frac{1}{\epsilon_-} = 0.063$ [61]
oxide second polar phonon energy	E=153 meV [61]
second polar optical constant	$\frac{1}{\epsilon_+} - \frac{1}{\epsilon_-} = 0.143$ [61]
oxide mean polar phonon energy	E=108 meV
mean polar optical constant	$\frac{1}{\epsilon_+} - \frac{1}{\epsilon_-} = 0.2$
oxide screening (miniband transport)	$k_D = 10^9$ cm^{-1}
electron density (WS transport)	$n = 10^{16}$ cm^{-3}
asymmetric superlattice device	
number of superlattice periods	20

Table C.1: *Values of the physical quantities used in the simulation.*

Physical quantity	**Value**
electron effective mass	$m^* = 0.067 m_0$
relative dielectric constant	$\epsilon_r = 13.18$
without SAW potential	
device length	600 nm
wires width	6 nm
barrier width	2 nm
quantum NOT window length	16 nm
beam splitter window length	8 nm
wave packet extension (eq.6.3)	$\sigma = 25$ nm
wave packet energy	35 meV
with SAW potential	
device length	600 nm
wires width	10 nm
barrier width	4 nm
quantum NOT window length	7 nm
beam splitter window length	5 nm
SAW wavelength	200 nm
sound velocity in GaAs	$v_s = 3.3 \times 10^5$ cm/s
SAW energy	200 meV

Table C.2: *Values used for quantum wires simulation.*

Bibliography

[1] P. Ball. *Nature*, 409:974, 2001.

[2] D. J. Lockwood. *Light Emission in Silicon: from Physics to Devices.* Academic Press, London, 1998.

[3] O. Bisi, S. U. Campisano, L. Pavesi, and F. Priolo. *Silicon Based Microphotonics: from Basics to Applications.* Ios Press, Amsterdam, 1999.

[4] O. Bisi, S. Ossicini, and L. Pavesi. *Surf. Sci. Reports*, 38:5, 2000.

[5] J. Feldmann, K. Leo, J. Shah, D. A. B. Miller J. E. Cunningham, G. von Plessen, A. Shulze, P. Thomas, and S. Shmitt-Rink. *Phys. Rev. B*, 46:7252, 1992.

[6] R. Tsu. *Nature*, 364:19, 1993.

[7] S. Ossicini, A. Fasolino, and F. Bernardini. *Phys. Rev. Lett.*, 72:1044, 1994.

[8] F. Arnaud d'Avitaya, L. Vervoort, F. Bassani, S. Ossicini, A. Fasolino, and F. Bernardini. *Europhys. Lett.*, 31:25, 1995.

[9] L. Vervoort, F. Bassani, I. Mihalchescu, J. C. Vial, and F. Arnaud d'Avitaya. *Phys. Stat. Sol. B*, 190:123, 1995.

[10] F. Bassani, L. Vervoort, I. Mihalchescu, J. C. Vial, and F. Arnaud d'Avitaya. *J. Appl. Phys.*, 79:4066, 1996.

[11] D. J. Lockwood, Z. H. Lu, and J. M. Baribeau. *Phys. Rev. Lett.*, 76:539, 1996.

[12] S. V. Novikov, J. Sinkkonen, O. Kilpela, and S. V. Gastev. *J. Vac. Sci. Tec. B*, 15:1471, 1997.

[13] E. Degoli and S. Ossicini. *Phys. Rev. B*, 57:14776, 1998.

[14] H. Kageshima and K. Shiraishi. *Phys. Rev. Lett.*, 81:5936, 1998.

[15] N. Tit and M. W. C. Dharma Wardana. *Sol. St. Comm.*, 106:191, 1998.

[16] A. G. Nassiopoulou, V. Ioannou-Sougleridis, P. Photopoulos, A. Travlos, V. Tsakiri, and D. Papadimitriou. *Phys. Stat. Sol. B*, 165:79, 1998.

[17] L. Tsybeskov, K. D. Hirschmann, S. P. Duttagupta, M. Zacharias, P. M. Fauchet, J. P. Mc Caffrey, and D. J. Lockwood. *Appl. Phys. Lett.*, 72:43, 1998.

[18] G. Pucker, M. Cazzanelli, P. Belletti, K. Gatterer, C. Spinella, and L. Pavesi. *J. Appl. Phys.*, 88:6044, 2000.

[19] V. Mulloni, R. Chierchia, C. Mazzoleni, G. Pucker, and L. Pavesi. *Phyl. Mag.*, 80:705, 2000.

[20] E. Degoli and S. Ossicini. *Surf. Sci.*, 479:32, 2000.

[21] Z. H. Lu and D. Grozea. *Appl. Phys. Lett.*, 80:255, 2002.

[22] A. G. Nassiopoulou, V. Tsakiri, V. Ioannou-Sougleridis, P. Photopoulos, S. Menard, F. Bassani, and F. Arnaud d'Avitaya. *J. Lumin.*, 80:81, 1998.

[23] S. Menard, M. Liniger, F. Bassani, F. Arnaud d'Avitaya, A. N. Kholod, and V. E. Borisenko. *Mat. Sci. Eng. B*, 69-70:464, 2000.

[24] P. Photopoulos, A. G. Nassiopoulou, D. N. Kouvastsos, and A. Travlos. *Appl. Phys. Lett*, 76:3588, 2000.

[25] P. Photopoulos, A. G. Nassiopoulou, D. N. Kouvastsos, and A. Travlos. *Mat. Sci. Eng. B*, 69-70:345, 2000.

[26] C. L. Heng, Y. K. Sun, T. Wang, Y. Chen, Y. P. Qiao, B. R. Zang, Z. C. Ma, W. H. Zong, and G .G. Qin. *Appl. Phys. Lett.*, 77:1416, 2000.

[27] G. Pucker, P. Bellutti, M. Cazzanelli, Z. Gaburro, and L. Pavesi. *Opt. Mat.*, 17:27, 2000.

[28] A. N. Kholod, A. L. Danilyuk, V. E. Borisenko, F. Bassani, S. Menard, and F. Arnaud d'Avitaya. *J. Appl. Phys.*, 85:7219, 1999.

[29] A. N. Kholod, V. E. Borisenko, A. Zaslavsky, and F. Arnaud d'Avitaya. *Phys. Rev. B*, 60:15975, 1999.

[30] T. Ouisse, V. Ioannou-Sougleridis, D. Kouvatsos, and A. G. Nassiopoulou. *J. Phys. D: Appl. Phys.*, 33:2691, 2000.

[31] C. B. Duke. *Tunneling in solids; Solid Physics Supplement 10.* Academic Press, New York, 1969.

[32] M. Lininger, A. N. Kholod, S. Menard, V. E. Borisenko, F. Bassani, G. Guirleo, and F. Arnaud d'Avitaya. *J. Appl. Phys*, 89:6281, 2001.

[33] A. Wacker. *Phys. Rep.*, 357:1, 2002.

[34] G. Bastard. *Wave Mechanics Applied to Semiconductors Heterostructures.* Les Edistions de Physique, Paris, 1990.

[35] L. J. Sham. Electronic Properties in Semiconductor Heterostructures. In P. Butcher, N. H. March, and M. P. Tosi, editors, *Physics of low-dimwnsional semiconductors structures.* Plenum Press, New York, 1993.

[36] M. Hirose. *Mat. Sci. Eng. B*, 41:35, 1996.

[37] B. Brar, G. D. Wilk, and A. C. Seabaugh. *Appl. Phys. Lett.*, 69:2728, 1996.

[38] H. Rücker, E. Molinari, and P. Lugli. *Phys. Rev. B*, 45:6747, 1992.

[39] E. Molinari and A. Fasolino. Phonons of ideal (001) superlattice: application to Si/Ge. In G. Fasol, A. Fasolino, and P. Lugli, editors, *Spectroscopy of Semiconductor Microstructures*. Plenum Press, New York, 1989.

[40] H. Haken. *Quantum Field Theory of Solids - An Introduction*. North Holland, Amsterdam, 1976.

[41] F. Bloch. *Z. Phys.*, 52:555, 1928.

[42] L. Esaki and R. Tsu. *IBM J. Res. Dev.*, 14:61, 1970.

[43] L. Reggiani. *Hot-Electron Transport in Semiconductors*. Springer, Berlin, 1985.

[44] C. Jacoboni and L. Reggiani. *Rev. Mod. Phys.*, 55:645, 1983.

[45] M. Rosini, C. Jacoboni, and S. Ossicini. *Phys. Rev. B*, 66:155332, 2002.

[46] A. Wacker, A.-P. Jahuo, S. Rott, A. Markus, P. Binder, and G. H. Dohler. *Phys. Rev. Lett.*, 83:836, 1999.

[47] E. E. Mendez, F. Agulló-Rueda, and J. M. Hong. *Phys. Rev. Lett.*, 60:2426, 1988.

[48] P. Yu and M. Cardona. *Fundamentals of Semiconductors*. Springer Verlag, Berlin, 1996.

[49] A. Bertoni, P. Bordone, R. Brunetti, C. Jacoboni, and S. Reggiani. *Phys. Rev. Lett.*, 84:5912, 2000.

[50] D. P. Di Vincenzo. Topics in quantum computers. In L. Kovenhoven, G. Schn, and L. Sohn, editors, *Mesoscopic electron transport - NATO ASI series E*. Kluwer, 1997.

[51] S. L. Braunstein, A. Mann, and M. Revzen. *Phys. Rev. Lett.*, 68:3259, 1992.

[52] C. C. Eugester, J. A. delAlamo, M. J. Rooks, and M. R. Melloch. *Phys. Rev. Lett.*, 64:3157, 1994.

[53] A. Bertoni, P. Bordone, R. Brunetti, C. Jacoboni, and S. Reggiani. *J. Mod. Opt.*, 49:1219, 2002.

[54] J. M. Shilton, V. I. Talyanskii, M. Pepper, D. A. Ritchie, J. E. F. Frost, C. J. B. Ford, C. G. Smith, and G. A. C. Jones. *J. Phys.: Condens. Matter*, 8:L531, 1996.

[55] V. I. Talyanskii, J. M. Shilton, M. Pepper, C. G. Smith, E. H. Linfield, C. J. B. Ford, D. A. Ritchie, and G. A. C. Jones. *Phys. Rev. B*, 56:15180, 1997.

[56] J. Cunningam, V. I. Talyanskii, J. M. Shilton, M. Pepper, M. Y. Simmons, and D. A. Ritchie. *Phys. Rev. B*, 60:4850, 1999.

[57] M. W. Keller, J. M. Martinis, N. M. Zimmerman, and A. H. Steinbach. *Appl. Phys. Lett.*, 69:1804, 1996.

[58] F. Reif. *Fundamentals of statystical and thermal physics*. Mc Graw-Hill, 1965.

[59] A. Dargys and J. Kundrotas. *Handbook of Physical Properties of Ge, Si, GaAs*. Science and Enciclopedia Publishers, Vilnius, 1994.

[60] J. B. Xia and K. W. Cheah. *Phys. Rev. B*, 56:14925, 1997.

[61] M. V. Fischetti and D. J. Di Maria. *Sol. St. El.*, 31:629, 1988.